COUPLED FLUID FLOW AND GEOMECHANICAL MODELING OF FAULT ACTIVATED INDUCED SEISMICITY

A Thesis

by

JOSHUA PRINCE EBIN

Submitted to the Office of Graduate and Professional Studies of
Texas A&M University
in partial fulfillment of the requirements for the degree of

MASTER OF SCIENCE

Chair of Committee,	Akhil Datta-Gupta
Co-Chair Committee,	Michael J. King
Committee Member,	Debjyoti Banerjee
Head of Department,	Jeff Spath

December 2018

Major Subject: Petroleum Engineering

ABSTRACT

Many unconventional shale applications in the oil and gas industry require coupling of reservoir fluid flow with geomechanics simulations for a holistic study of formation stability. Since traditional reservoir simulation packages normally do not fully support geomechanical effects resulting from pore pressure change and varying stress states, finite difference flow simulators which handle multi-phase regimes with varying fluid saturations need to be supplemented with finite element analysis software applications that include geomechanics capabilities but might be limited to single phase fluid flow regimes. The general theme in events leading to induced seismicity from human interaction with the environment involves pore pressure, strain change, total stress and effective stress variations in a reservoir system with underlying faults, undergoing fluid injection and extraction. The objective of the current research study is to couple fluid flow with geomechanical effects to model pore pressure, stress variations and strain change using commercially available finite element analysis in Abaqus and finite difference analysis in CMG for comparison. Reservoir material properties and output strain results from both CMG and Abaqus coupled models are used to calculate induced seismic moments during unbalanced waste water injection and brine production in a reservoir system with an underlying fault. Results suggest that a combination of fluid flow and geomechanics can have an impact on induced seismicity. Near fault basement strain change depends more on production pattern compared to injection pattern variations as more compaction occurs. Unbalanced target formation injection-production activity can lead to increased strain change and seismicity in the basement. Induced seismicity is more related to strain change as opposed to pore pressure change for the cases studied here.

DEDICATION

I dedicate this work to God, my parents, family and friends who have supported me in many ways throughout my academic career.

ACKNOWLEDGEMENTS

I would like to thank my advisor, Dr. Datta-Gupta, and my committee members, Dr. king and Dr. Banerjee for their support, guidance and encouragement throughout the course of this research.

I would also like to appreciate Dr. Morita for making time to discuss general concepts related to my research. Thanks to my research group mentors, Jaeyoung Park, Rongqiang Chen, Xu Xue, and Atsushi Lino for their support and willingness to answer questions related to the research work.

I would like to thank Dr. Merriweather and Dr. Walton from the Texas A&M Louise Stokes Alliance for Minority Participation- Bridge to Doctorate Program (LSAMP-BTD) for the opportunity to be interviewed and selected for the BTD fellowship which allowed me to work on this research. This work would not have been possible without their support.

Thanks to my friends, colleagues, research group, department faculty, staff and the TAMU SPE family for making my time at Texas A&M University a memorable experience.

Finally, thanks to my mother, father, siblings and my best friend, Adaku, for their patience with me accompanied with constant motivation and encouragement.

CONTRIBUTORS AND FUNDING SOURCES

This work was supported by a thesis committee consisting of Dr. Datta-Gupta (advisor), Dr. King (co-advisor) of the petroleum engineering department, and Dr. Banerjee of the department of Mechanical Engineering.

This Master's thesis research work was supported by funding from the Louise Stokes Alliance for Minority Participation- Bridge to Doctorate (LSAMP-BTD) fellowship at Texas A&M University. The work presented is a continuation of a previous geomechanics research carried out by Jaeyoung Park and Rongqiang Chen of the Model Calibration Efficient Reservoir Imaging (MCERI) research group in the petroleum engineering department at Texas A&M University. The comparison of two geomechanics simulation methodologies in chapter II, analyses results in chapters III through IV and conclusions in chapter V are new contributions to the research progress.

NOMENCLATURE

ϕ°	Angle of internal friction
u_a	Average pressure in non-wetting fluid
u_w	Average pressure in wetting fluid
α	Biot coefficient (Biot Number)
B	Body force
b	Body force per unit mass of fluid
$\vec{f}$	Body force per unit volume
K	Bulk modulus (incompressibility)
V_b	Bulk volume
$\vec{\sigma}$	Cauchy stress tensor
μ	Coefficient of friction
S_o	Cohesion
ρ	Density
u	Displacement
σ_n'	Effective normal stress
τ_n'	Effective shear stress
$\vec{\sigma}'$	Effective stress tensor
J	Elastic volume ratio
c_f	Fluid compressibility

p	Fluid pressure
$\vec{V}_w$	Fluid velocity
F	Force
B	Formation volume factor
F_r	Frictional reaction force
g	Gravitational constant
Ƙ	Hydraulic conductivity
I	Identity matrix
N^N, B^N	Lagrangian interpolation functions
L	Longitudinal lateral length
σ'_m	Mean effective stress
f_N	Normal force
N_n	Number of grids in the nth direction
k	Permeability
v	Poisson ratio
δP_w	Pore pressure variational field test function
ϕ	Porosity
ϕ^*	Reservoir porosity (coupling term)
c_R	Rock compressibility
χ	Saturation

M_o	Seismic moment intensity
M_w	Seismic moment magnitude
$\vec{M}_{pq}$	Seismic moment tensor
$\gamma_{s_{ij}}$	Shear strain
q	Source sink term
g	Specific gravity
ϵ	Strain
Δe_{rs}	Strain change
σ	Stress
$\square_{f,R,M,e,i}$	Subscripts: fluid, rock, matrix, element, initial
υ	Superficial velocity
A	Surface area
$\vec{t}$	Surface tractions tensor per unit area
$\vec{C}$	Tangential stiffness tensor
t	Time
n_f	Total wetting fluid volume (free +trapped) per unit volume in current config
T	Traction or tractive force
$\vec{n}$	Unit normal
β	Velocity coefficient

$\delta\vec{\varepsilon}$	Virtual rate of deformation
$\delta\vec{\mathrm{v}}$	Virtual velocity field
μ_f	Viscosity of fluid
e	Void ratio
V	Volume
n_t	Volume ratio of trapped fluid at a point
n_w	Volume ratio of free wetting fluid
$\overrightarrow{\dot{Q}}$	Volumetric flow rate per unit area of a particular wetting fluid
ϵ_v	Volumetric strain
E	Young’s modulus

TABLE OF CONTENTS

Page

LIST OF FIGURES

Page

LIST OF TABLES

Page

CHAPTER I

INTRODUCTION AND LITERATURE REVIEW

1.1 Introduction

Many unconventional shale applications in the oil and gas industry require coupling of reservoir fluid flow with geomechanics simulations for a holistic study of pore pressure, stress variations and strain change which affect formation stability. In order to understand the complex phenomena associated with Induced seismic activity, the combination of reservoir fluid flow with stress models are necessary, especially in unconventional applications that involved fluid extraction and injection. Common problems that can be examined with the help of geomechanics include subsidence, reservoir compaction drive, casing failure, wellbore stability, sand production, fault activation, and pore collapse failure among others. Seismic data available from the Berkeley Seismology Lab suggests that there has been a recent increase in seismic activity in the US mid-western states like Oklahoma, and Texas among others. The hockey stick curve in Fig. 1 illustrates the increase in recorded seismic activity of seismic moment magnitude,$M \geq 3$, from $1973 - 2016$. As indicated by the red portion of the curve, the last seven years have seen an enormous increase in recorded seismic events in US mid-western states. Most of these recorded seismic activities are attributed to human activities. Since traditional reservoir simulation packages normally do not fully support geomechanical effects resulting from pore pressure change and varying stress states, finite difference fluid flow simulators which handle multi-phase regimes with varying fluid saturations need to be supplemented with finite element analysis software applications that include geomechanics capabilities but might be limited to single phase fluid flow regimes. The combination of reservoir fluid flow with stress models can help to better explain energy development processes and phenomena that involve fluid extraction and injection.

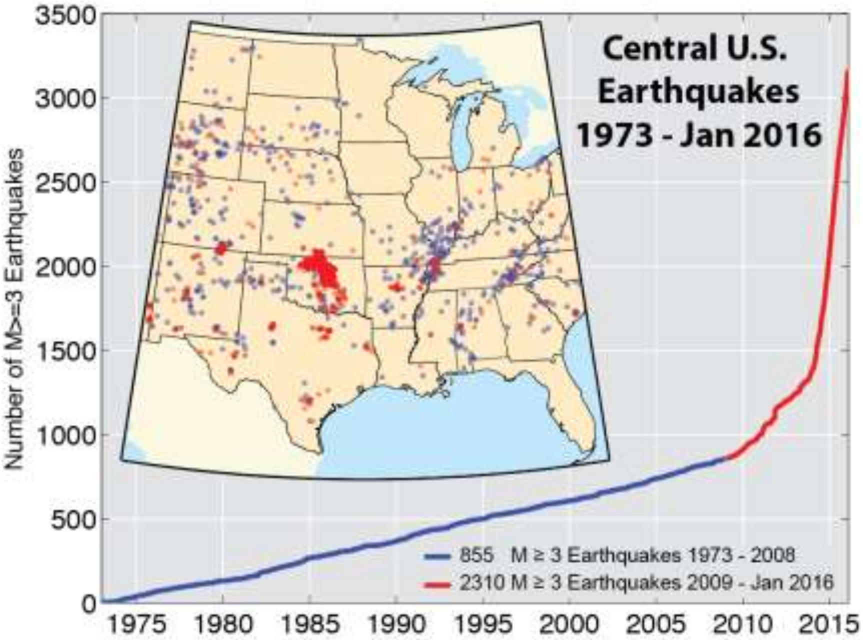

Fig. 1– Seismicity Increase in Mid-Western States (Adapted from Rubinstein, 2015)

1.2 Background

Induced seismicity can be defined as low magnitude earthquakes and tremors observed along a fault system as a result of human activity which alter the stress-strain response of the earth crust. Human activities which could alter stress-strain response include: waste water injection into deep disposal wells, CO_2 injection during storage in carbon capture sequestration, geothermal energy development, and other energy technologies that require fluid injection and extraction from deep within the earth's crust. Changes in loading conditions such as fluid-pressure diffusion, gravitational loading or poro-thermo-elastic effects on a pre-existing underlying fault can lead to induced seismicity. Fig. 2 below illustrates the effects of fluid injection and withdrawal on nearby faults which can trigger induced seismicity (United States Geological Survey, USGS 2015). On the left side portion of the figure below, direct loading by fluid injection near a fault in a high permeability region increases the pore pressure which leads to stress alteration. On the right side portion of the figure, an indirect loading from the changes in the solid stress due to fluid injection and extraction lead to near fault stress change. These stress alteration mechanisms could lead to sudden movement along the fault slip thereby inducing seismic activity.

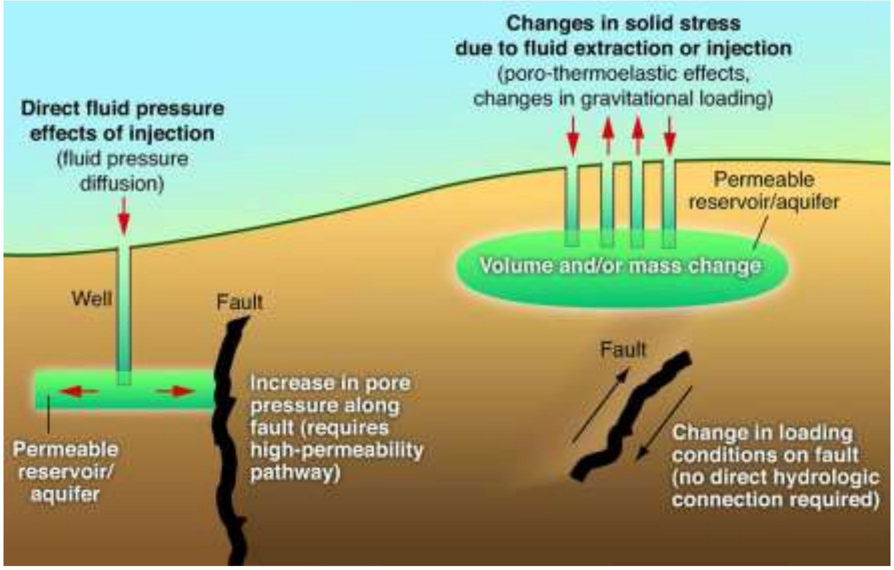

**Fig. 2 – Effects of Fluid Injection and Withdrawal on Nearby Faults
(Adapted from Rubinstein, 2015)**

Water column changes in large deep artificial lakes can induce pore pressure and total stress increase thereby yielding effective stress variations on underlying faults resulting in earthquakes (Simpson et al., 1988). Post mining voids in rock can collapse or alter the natural rock force balance, produce seismic waves and in some cases reactivate existing faults causing minor earthquakes (Redmayne 1988). Injection of large volumes of produced water (high saline fluid from oil and gas wells) into waste disposal wells increases the subsurface pore pressure and has been identified as a trigger for fault slips resulting in earthquakes (Frohlich et al., 2009). Gonzalez et al., (2012) illustrate how changes in crustal stress response due to large scale extraction of groundwater can trigger earthquakes as in the case of the 2011 Lorca earthquake. The general theme in events leading to induced seismicity from human interaction with the environment involves pore pressure, strain change, total stress and effective stress variations in a reservoir system with underlying faults, undergoing fluid injection and extraction. A coupled fluid flow with

Geomechanics model is necessary to fully capture stress, strain response and resultant induced seismicity. Geomechanical analysis of fluid injection and seismic fault slip by (Fan et al., 2016) show that low fault permeability favors fault reactivation which is also sensitive to fault orientation, stress state, reservoir permeability and results indicate injection-induced fault slip plausible for Timpson M_w 4.8 earthquake sequence. (Hornbach et al., 2015) used pore pressure modeling studies to indicate brine production and waste water disposal as likely cause for a series of seismic events recorded along a fault system near Azle, Texas. However, in the Azle case, Geomechanics and seismic moment magnitude were not included. Coupled fluid flow with geomechanics techniques are necessary for problems that involve compaction drive, subsidence, gas hydrate deposits, well failure, geothermal and shale/ tight gas reservoirs among others.

1.3 Research Objectives

The objective of the current research study is to couple fluid flow with Geomechanical effects to model pore pressure, strain change using commercially available finite element analysis in Abaqus and finite difference analysis in CMG for comparison. Reservoir material properties and output strain results from both CMG and Abaqus coupled models are used to calculate induced seismic moments during unbalanced waste water injection and brine production in a reservoir system with an underlying fault. The test models used for this study in Abaqus and CMG are developed with a similar reservoir grid structure and setup to the Azle case assuming one injection and one production well and a uniform single block in the y direction. Strain change in the basement formation are investigated in response to unbalanced production-injection patterns in a nearby target formation.

CHAPTER II

COUPLED FLUID FLOW WITH GEOMECHANICS METHODOLOGY

2.1 Governing Geomechanics Equations

In terms of geomechanics, fundamental properties including stress(σ), strain (ϵ) and displacement (u) are commonly used. The traction or tractive force (T) used to generate motion between a body and a tangential surface through the use of dry friction or the shear force of a surface can be defined as force (ΔF) per unit area (ΔA).

$$T = \lim_{\Delta A \to 0} \left(\frac{\Delta F}{\Delta A} \right) \tag{1}$$

Assuming $\vec{n}$ is the unit normal vector to the area, the stress tensor $(\vec{\sigma})$ can be defined in terms of the traction force as follows:

$$T = \vec{n}.\, \vec{\sigma} \tag{2}$$

The stress tensor components in matrix form are written as follows:

$$\vec{\sigma} = \sigma_{ij} = \begin{bmatrix} \sigma_{11} & \sigma_{12} & \sigma_{13} \\ \sigma_{21} & \sigma_{22} & \sigma_{23} \\ \sigma_{31} & \sigma_{32} & \sigma_{33} \end{bmatrix} \tag{3}$$

Where the subscripts $i\ and\ j$ for σ_{ij} refers to the traction acting on the surface perpendicular to the i axis while the direction of the traction is in the j direction. The effective stress (σ') commonly referred to as the average normal force per unit area transmitted from grain to grain is defined as follows:

$$\vec{\sigma}' = \vec{\sigma}_t - \alpha pI \tag{4}$$

The above assumes a compressive positive sign convention where σ_t is the total stress, I is the identity matrix, p is the pore pressure, and α is the biot number (coefficient or constant) which is a factor describing the form of fluid-solid coupling ranging from rock porosity ϕ to 1 based on the bulk modulus (K). This is because, theoretically, the lower and upper limits of the drained bulk modulus are 0 and $(1-\phi)K_{solid\ material}$ respectively (Fjaer et al., 1992).

$$\alpha = 1 - \frac{K_{drained}}{K_{solid\ material}} \tag{5}$$

In unconsolidated (weak) rock, the biot constant approximately approaches unity whereas in consolidated (solid) rock, the biot constant approximately approaches the rock porosity. The drained bulk modulus is always less than the solid material bulk modulus. Drained conditions apply when the total stress is entirely supported by a solid framework such that the pressure remains constant as fluid is allowed to escape a system while loading. On the other hand, undrained conditions apply when the total stress is supported partial both by a solid framework and by a fluid. The mean effective stress $(\sigma_m{}')$ is defined as a function of the principal effective stress components in each coordinate direction:

$$\sigma_m^{'} = \frac{1}{3}\sigma_{ii}^{'} = \frac{1}{3}\left(\sigma_{11}^{'} + \sigma_{22}^{'} + \sigma_{33}^{'}\right) \tag{6}$$

The principal effective stress occurs when the traction force is parallel to the unit normal vector. The above mean effective stress expression assumes no shear stresses occur and the maximum principal stress corresponds to σ_{11}' while the minimum principal stress corresponds to σ_{33}' .

The displacement of a body can be described by the change in body shape and location from a reference configuration (initial body state) to a deformed configuration (current body state) as a result of the forces acting on it. The displacement can be considered in terms of the sum of deformation caused by stress change and deformation due to rigid body motion (translation or rotation). The displacement vector, $\vec{u} = f(\vec{x}, t)$ is a function space and time (t) such that the position of the particle can be described by a vector in space, $\vec{x} = \{x_1, x_2, x_3\}$ for the corresponding $\vec{u} = \{u_1, u_2, u_3\}$.

The strain is measure for the deformation observed in a material which can be normal or shear strains. The normal strain is defined as the change in length per unit length while the shear strain is defined as the change in angle between two original orthogonal directions. Rigorously, the normal strain, assuming only translation, can be derived by geometric relations by considering limit of the ratio of the change in dimension to original dimension of a simple square strip element as follows:

$$\varepsilon_{**} = \lim_{\Delta x_* \to 0} \left(\frac{\Delta x_* + \left(\frac{du_*}{dx_*} \right) \Delta x_* - \Delta x_*}{\Delta x_*} \right) \approx \frac{du_*}{dx_*} \qquad (7)$$

Where $* = 1, 2, or\ 3$ is the axis direction of interest, u here is a simple linear axial displacement function and x is the position vector component of the square strip point in space. Using the same logic for all normal directions, the normal strain components become:

$$\varepsilon_{11} = \frac{du_1}{dx_1}; \varepsilon_{22} = \frac{du_2}{dx_2}; \varepsilon_{33} = \frac{du_3}{dx_3} \qquad (8)$$

Similarly, the shear strain (γ_s), accounting for rotation, can be derived by geometric relations by considering limit of the angle between two original orthogonal directions for a simple square strip element as follows:

$$\gamma_{s_{ij}} = \lim_{\Delta x_i,\, \Delta x_j \to 0} \left(\frac{\pi}{2} - \left[\frac{\pi}{2} - \frac{\left(\frac{du_j}{dx_i}\right)\Delta x_i}{\Delta x_i} - \frac{\left(\frac{du_i}{dx_j}\right)\Delta x_j}{\Delta x_j} \right] \right) \approx \frac{\partial u_i}{\partial x_j} + \frac{\partial u_j}{\partial x_i} \qquad (9)$$

Where the subscripts $i\ and\ j$ for $\gamma_{s_{ij}}$ refers to the shear acting on the surface perpendicular to the i axis while the direction of the shear is in the j direction. u remains the simple linear axial displacement function and x remains the position vector component of the square strip point in space. Using the same logic for all strain directions, the shear strain components become:

$$\begin{aligned} \grave{o}_{12} &= \frac{1}{2}\gamma_{12} = \frac{1}{2}\left(\frac{\partial u_1}{\partial x_2} + \frac{\partial u_2}{\partial x_1}\right) = \grave{o}_{21} \\ \grave{o}_{13} &= \frac{1}{2}\gamma_{13} = \frac{1}{2}\left(\frac{\partial u_1}{\partial x_3} + \frac{\partial u_3}{\partial x_1}\right) = \grave{o}_{31} \\ \grave{o}_{23} &= \frac{1}{2}\gamma_{23} = \frac{1}{2}\left(\frac{\partial u_2}{\partial x_3} + \frac{\partial u_3}{\partial x_2}\right) = \grave{o}_{32} \end{aligned} \qquad (10)$$

Then, the strain tensor $\vec{\epsilon}$ components in matrix form assuming symmetry is written as follows:

$$\vec{\grave{o}} = \grave{o}_{ij} = \begin{bmatrix} \grave{o}_{11} & \grave{o}_{12} & \grave{o}_{13} \\ \grave{o}_{21} & \grave{o}_{22} & \grave{o}_{23} \\ \grave{o}_{31} & \grave{o}_{32} & \grave{o}_{33} \end{bmatrix} = \begin{bmatrix} \frac{du_1}{dx_1} & \frac{1}{2}\left(\frac{\partial u_1}{\partial x_2} + \frac{\partial u_2}{\partial x_1}\right) & \frac{1}{2}\left(\frac{\partial u_1}{\partial x_3} + \frac{\partial u_3}{\partial x_1}\right) \\ \frac{1}{2}\left(\frac{\partial u_1}{\partial x_2} + \frac{\partial u_2}{\partial x_1}\right) & \frac{du_2}{dx_2} & \frac{1}{2}\left(\frac{\partial u_2}{\partial x_3} + \frac{\partial u_3}{\partial x_2}\right) \\ \frac{1}{2}\left(\frac{\partial u_1}{\partial x_3} + \frac{\partial u_3}{\partial x_1}\right) & \frac{1}{2}\left(\frac{\partial u_2}{\partial x_3} + \frac{\partial u_3}{\partial x_2}\right) & \frac{du_3}{dx_3} \end{bmatrix} \qquad (11)$$

The volumetric strain is the ratio of the change in current bulk volume (V_b) to initial bulk volume (V_b^i) which is therefore:

$$\grave{o}_v = \frac{V_b^i - V_b}{V_b^i} = \grave{o}_{11} + \grave{o}_{22} + \grave{o}_{33} \tag{12}$$

Assuming a homogenous, isotropic and symmetric system, the geomechanical formulation begins with the classic force equilibrium equation which postulates that the sum of all normal, shear and body forces should equal zero.

$$\nabla . \vec{\sigma} - B = 0 \tag{13}$$

Where $\vec{\sigma}$ represents the total stress tensor acting one direction and B represents the body forces due to gravity acting in the opposite direction with respect to total stresses. The strain tensor $(\vec{\epsilon})$ is defined as occurring due to deformations in the length and shape of a body according to the following kinematic strain-displacement equation approximated from the Green-lagrange infinitesimal strain tensor:

$$\vec{\sigma} = \frac{1}{2}\left[\nabla \vec{u} + \left(\nabla \vec{u} \right)^T \right] \tag{14}$$

Where u is the displacement vector which locates a rock particle in space connecting the position of the particle in a reference Cartesian coordinate system to its new position in a deformed Cartesian coordinate system. The strain is considered small and much less than 1. The constitutive stress-strain relationship applies as follows:

$$\vec{\sigma} = \vec{C} : \vec{\sigma} + \alpha \text{ p I} \tag{15}$$

Where $\vec{C}$ is the tangential stiffness tensor, α is the biot coefficient, p is the fluid pressure and I is the identity matrix. The above expression neglects the contribution from the thermo-elastic-temperature term and only considers the pore pressure contribution. By substituting and combining the force equilibrium, kinematic-strain displacement and constitutive stress-strain relationships, a solution can be obtained and implemented as the final geomechanics solution for a deformable medium.

$$\nabla\left[\vec{C}:\left(\frac{1}{2}\left(\nabla u+\left(\nabla u\right)^{T}\right)\right)\right]=-\nabla\alpha\ \mathrm{p}\ \mathrm{I}+\rho\mathrm{g} \tag{16}$$

Once again, the above solution does not account for energy conservation because the reservoir temperature variation in this study is assumed to be insignificant. The tangential stiffness tensor can be expressed in various forms. One common form is expressed as a function of the Young's Modulus and the Poisson's ratio as follows:

$$\vec{C}=\frac{E\left(1-v\right)}{\left(1+v\right)\left(1-2v\right)}\begin{bmatrix} 1 & \frac{v}{\left(1-v\right)} & \frac{v}{\left(1-v\right)} & 0 & 0 & 0 \\ \frac{v}{\left(1-v\right)} & 1 & \frac{v}{\left(1-v\right)} & 0 & 0 & 0 \\ \frac{v}{\left(1-v\right)} & \frac{v}{\left(1-v\right)} & 1 & 0 & 0 & 0 \\ 0 & 0 & 0 & \frac{\left(1-2v\right)}{2\left(1-v\right)} & 0 & 0 \\ 0 & 0 & 0 & 0 & \frac{\left(1-2v\right)}{2\left(1-v\right)} & 0 \\ 0 & 0 & 0 & 0 & 0 & \frac{\left(1-2v\right)}{2\left(1-v\right)} \end{bmatrix} \tag{17}$$

The biot coefficient can be obtained as a function of the tangential stiffness tensor, poison's ratio, and Young modulus of the rock matrix as follows:

$$\alpha = 1 - \frac{1}{3}\left[\frac{3(1-2v_m)}{E_m}\right] \tag{18}$$

For a 1D problem, the tangential stiffness tensor simply becomes the same value as the Young's Modulus. Given the applied body force alongside other input parameters, the displacement, strain tensor and stress tensor components can be calculated.

Basic input materials properties involved in this study include: Young's Modulus(E), Poisson's ratio(v), bulk modulus(K), and angle of internal friction(ϕ°). The Young's Modulus is a ratio of the extension in a material under the influence of laterally (diameter direction for cylindrical rods) unrestricted axial tension. By the Hooke's Law definition, the Youngs Modulus is a ratio between the stress and lateral strain:

$$E = \frac{\sigma}{\varepsilon_{longitudinal}} = \frac{F / A}{\Delta L / L} \tag{19}$$

Where F, A, L are the force, surface area, and longitudinal lateral length respectively. The Poisson's ratio is defined as the ratio of lateral contraction to longitudinal extension strains.

$$v = \frac{-\varepsilon_{lateral}}{+\varepsilon_{longitudinal}} = -\frac{\varepsilon_d}{\varepsilon_l} \tag{20}$$

Where the negative sign is indicative of the contraction which occurs in the lateral direction. The bulk modulus (K) is the defined as the ratio of the hydrostatic pressure to the volumetric strain:

$$K = \frac{\sigma_p}{\varepsilon_v} = \frac{\sigma_p}{\varepsilon_{11} + \varepsilon_{22} + \varepsilon_{33}} \tag{21}$$

By substituting, the above material equations into one another, a convenient expression which summarizes the relationship among the Young Modulus, Elastic Modulus, and Poisson ratio is given by:

$$K = \frac{E}{3(1-2v)} \tag{22}$$

2.2 Coupled Fluid Flow with Geomechanics Approach

In this chapter, various coupling techniques are outlined and the need for a fully coupled or equivalent fluid flow with geomechanics model is explained in detail. Before discussing the various coupling methods and the reasons for the method of choice, a brief overview of the basic equations for porous media fluid flow is outlined. The basic equations for porous media fluid flow consists of Darcy's Law, mass conservation (material balance), energy conservation as well as the equations of state equations which describe the fluid characteristics. Darcy's law which relates the apparent superficial velocity (υ) to the fluid pressure (p) is given by:

$$\upsilon = -\frac{k}{\mu_f}\nabla p \tag{23}$$

Where μ_f, k are fluid viscosity and permeability respectively. The above version of Darcy's law assumes a non-Darcy coefficient (δ) of 1 for fluids deviating from ideal conditions. The simplified material balance (continuity) equation for a single phase fluid assumed in this case is given by:

$$\frac{\partial(\phi\rho)}{\partial t} = \nabla\cdot(\rho\upsilon) + q \tag{24}$$

The above assumes a homogenous and isotropic reservoir system, neglecting the effect of gravity with constant reservoir and fluid properties. For a slightly compressible fluid, the reservoir fluid density (ρ) and formation volume factor $\left(B_f\right)$ can be described as functions of fluid pressure at a current and initial states as well as fluid compressibility.

$$\rho = \rho_i\left[1 + c_f\left(p - p_i\right)\right] \tag{25}$$

$$B_f = \frac{B_{f_i}}{\left[1 + c_f \left(p - p_i\right)\right]} \qquad (26)$$

If the rock is assumed to be slightly compressible rock, then the porosity varies with pressure. Hence the rock compressibility (c_R) is given by:

$$c_R = \frac{\left(\frac{\phi}{\phi_i} - 1\right)}{p - p_i} \qquad (27)$$

The fluid flow equations can then be solve by conventional flow simulators. However, conventional flow simulators typically assume that the porous media grid is does not deform which is rigorously not the case in reality. This implies that for a grid cell with fixed bulk volume, conventional flow simulators ignore any bulk medium movement that accompanies rock expansion and contraction whereas geomechanical simulators do account for the porous media deformation to some extent (Denney et al 2006). The conservation principle needs to be modified in order to account for deformations. The formulation here assumes that the simulator grid is attached and deforms with the porous medium such that the previously definition bulk volume and volumetric strain apply equally to all grid cells in the simulated system.

The conservation of fluid in a deformable porous medium (Tran et al 2005) is given by:

$$\frac{\partial}{\partial t}\left[\phi \rho_f \left(1 - \epsilon_v\right)\right] - \nabla \,.\left(\rho_f \frac{k}{\mu}.\left[\nabla p - \rho_f b\right]\right) = Q_f \qquad (28)$$

Where ρ_f is the fluid density, ϵ_v is the volumetric strain, b is the body force per unit mass of fluid, k is the permeability, μ_f is the fluid viscosity, Q_f is the flow rate of fluid at source or sink location, and $\phi = \frac{V_p}{V_b}$ is the true porosity (Settari et al 1998) defined as the ratio of the current pore volume to the current bulk volume.

The volumetric strain defined in the altered mass conservation flow equation allows the conservation principle to account for the changes in the porous media bulk volume. In order to incorporate the porous media deformation into a conventional simulator, Tran et. al (2005) propose a “reservoir porosity” term (ϕ^*) which is a function of the volumetric strain to replace the true porosity in the altered mass conservation principle equation.

$$\phi^* = \left(1 - \varepsilon_v\right)\phi \tag{29}$$

Therefore the altered mass conservation equations which can be implemented as the final fluid flow equation in a conventional simulator becomes:

$$\frac{\partial}{\partial t}\left[\phi^* \rho_f\right] - \nabla \cdot \left(\rho_f \frac{k}{\mu_f} . \left[\nabla p - \rho_f b\right]\right) = Q_f \tag{30}$$

The above expression now accounts for the porous media deformation by virtue of the reservoir porosity term which acts as the link (coupling parameter) between the fluid flow and geomechanics equations in CMG.

In a similar fashion, the energy conservation principle for a reservoir system with time variant temperatures can be described as a function of the reservoir porosity term.

$$\frac{\partial}{\partial t}\left[\phi^* \rho_f U_f + \left(1 - \phi^*\right)\rho_r U_r\right] + \nabla \cdot \left[-\rho_f \frac{k}{\mu_f} . \left[\nabla p - \rho_f b\right] H_f\right] + \nabla \cdot \left[\kappa \nabla \mathrm{T}\right] = Q_h \tag{31}$$

Where Q_h is the heat loss/gain, T is the temperature, κ is the thermal conductivity, ρ is density while U_f and U_r are the fluid and rock enthalpies respectively. However, in this study the energy conservation principle is not employed because it is assumed that temperature changes over time are insignificant which may not necessarily be the case in reality. Several numerical methods for coupling geomechanics to fluid flow have been proposed in the literature. The most common coupling methods include: Explicit (One-way) coupling, Iterative (Two-way) coupling, and Fully coupled (Fully implicit) methods in increasing order of rigor. These methods are henceforth described from a reservoir geomechanics engineering perspective. The explicit coupling method involves solving the reservoir module equations and then using fluid flow results to solve the equations in the geomechanics module without feedback to the reservoir module. The explicit coupling approach can be viewed as a special case of the iterative coupling method because the reservoir flow remains unaffected by the geomechanical response since there is no feedback from the geomechanical module returning to the reservoir module. The transfer of information from the reservoir to geomechanics modules in the explicit approach is only via the fluid pressure because the fluid flow calculations are independent of the geomechanics response during the simulation. However, a change in the initial reservoir flow variables will change the geomechanics variables. The explicitly coupled approach is useful for example in a simple empirical compaction model where observed fluid pressure is matched to field data and then a separate geomechanics module is then used to calculate field deformation. Fig. 3 summarizes the workflow for the explicitly coupled approach. A disadvantage of explicit coupling is stability and accuracy issues as a result of imposed time step restrictions.

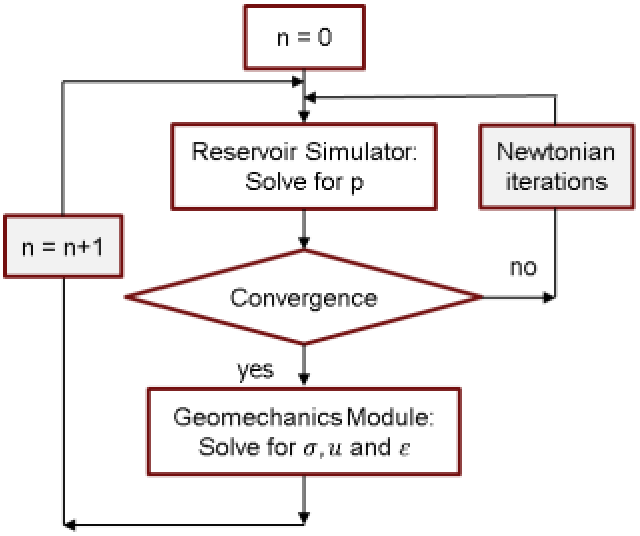

Fig. 3 – Explicit (One-Way) Coupling Schematic

The iteratively coupling method involves solving the geomechanics equations immediately after the reservoir equations and then exchanging results back and forth via a coupling parameter until the simulation is complete. The advantage of the iteratively coupled approach is widely used for modularity and flexibility because the coupling between the reservoir and geomechanics module subroutines can be done without considerably modifying both codes. In terms of modularity, for example, the fluid flow and geomechanics modules can be discretized in different ways including finite difference volume based grids and finite element nodal-based grids. However, for large complex difficult problems, the iterative coupling method may require a large number of iterations due to convergence rate issues with non-linear iterations. Here, the transfer of information back and forth between the reservoir simulator fluid flow module and the geomechanics simulator module is made possible by the previously discussed "reservoir porosity" coupling parameter,ϕ^*, and fluid pressure. Changes in permeability with stress and strain can be measured by laboratory experiments and determined as a function of porosity or volumetric strain or mean stress. The absolute permeability due to shearing can be defined as a function of volumetric strain from (Li et al., 2006) as follows:

$$\ln\left(k / k_0\right) = C_{n1}\epsilon_v \tag{32}$$

Where k and k_0 are respectively the permeability at the current sheared and initial conditions, ϵ_v is the volumetric strain, and C_{n1} is a constant known as the Touhidi-Baghini parameter which can be determined as described in Appendix A. Fig. 4 summarizes the workflow for the iteratively coupled approach. The subscripts n refers to the time step. Additional Newtonian coupling iterations can be used to refine the geomechanics response of the next time step. The coupling parameter is updated at the end of the geomechanical module calculations for each time step in such a manner that the conservation principle remains satisfied.

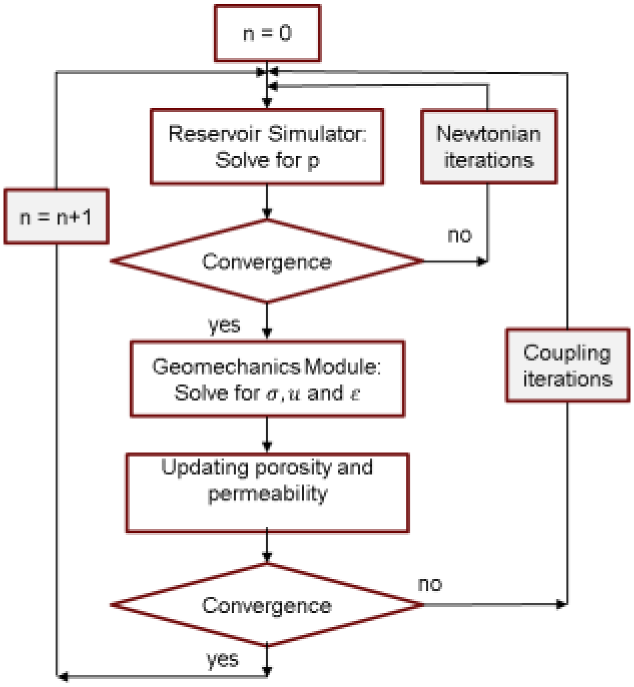

Fig. 4 – Iterative (Two-Way) Coupling Schematic

The fully coupled method has the most rigor and involves solving the reservoir and geomechanics equations simultaneously for fluid flow (pressure, temperature, saturations, composition) and deformation (displacement, strain, stress) variables. The coupling parameters between the fluid flow simulator module and the geomechanics module are solved at each time step and compared to the next time step until the difference is neglible or below a defined threshold (porosity for CMG) and (void ratio for Abaqus). Although, the fully coupled approach is more stable, reliable due to its rigor and suitable convergence for non-linear iterations, it is computationally expensive, requires more code development and is not always used for non-linear, large scale simulation problems. Fig. 5 summarizes the fully coupled strategy.

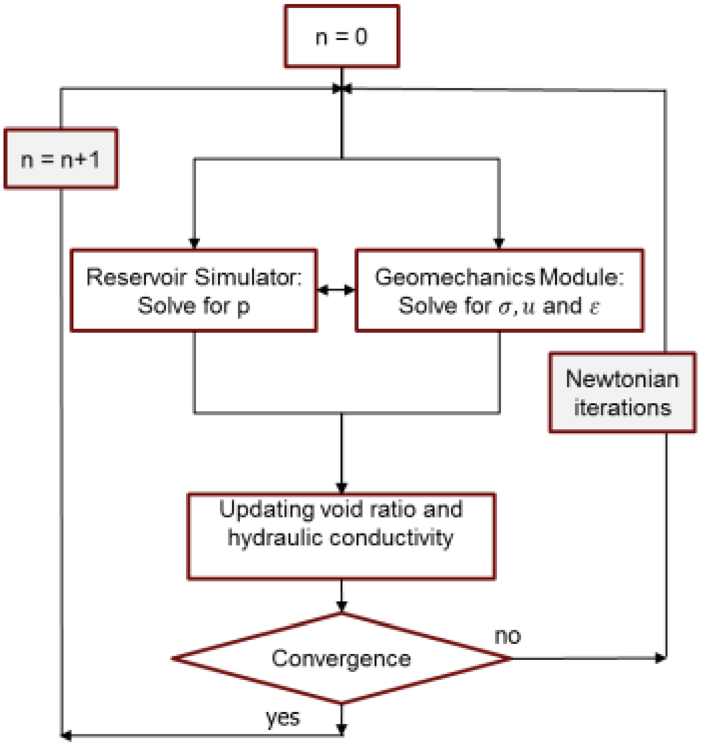

Fig. 5 – Fully Coupled Schematic

Other less common coupling strategies are loosely (pseudo) coupled and co-simulation strategies. The coupling between the reservoir and geomechanics module in the loosely coupled approach is resolved only after a certain number of time steps to save computational cost but is less reliable (Dean et al 2006). For the co-simulation strategy, results from a reservoir simulator (e.g Eclipse) are imported into another simulator for the subsequent geomechanical computations (e.g Abaqus 2014 documentation). In this study, the coupling strategy between reservoir and geomechanics module is the iteratively coupled approach for CMG and the fully coupled approach for Abaqus. CMG employs a sequentially iterative coupling (Two-Way) strategy. The pressure output from the reservoir module is sent to the geomechanics module. In the geomechanics module, the computed displacement, stress and strain are then used to determine the new pore compressibility and absolute permeability. Fluid flow and geomechanics are solved sequentially, update each other and coupled iteratively. This iteration between the reservoir and stress solution is performed until updated pore volume and permeability in both fluid flow and geomechanics models are similar. When iterative coupling converges, the results are sometimes similar to that of a fully coupled model if both techniques use sufficiently tight convergence tolerances for iterations (Dean et al). Changes in porosity involve fluid compressibility and geomechanical parameters such as Young's Modulus (E) , Poisson's ratio (v) and the Biot Coeffient (α).

Table 1 summarizes the key features of the main coupling strategies discussed based on literature (Minkoff et al., 2003; Tran et al., 2004, 2005; Dean et al., 2006; Jha et al., 2007; Abaqus 2014). Coupling formulation and discretization details for CMG and Abaqus are provided in Appendix A and B respectively.

Table 1 – Summary of Fluid Flow and Geomechanics Coupling Strategies

METHODS	RIGOR	COMPUTATIONAL COST	FLEXIBILITY	TRANSFER PARAMETER	STABILITY
One-Way	Low	Low	Medium	Fluid pressure	Low
Two-Way	Medium	Medium	High	Porosity	Medium
Fully Coupled	High	High	Low	Void Ratio	High
Loosely Coupled	Low	Low	Medium	Fluid Pressure	Medium

The second commercial software used for geomechanics- fluid flow coupling is Abaqus which is a general finite element package used to numerically solve partial differential equations. The coupled pore fluid diffusion and stress analysis method is performed in Abaqus using the 8-node trilinear displacement and pore pressure (C3D8P) finite elements. In Abaqus, the fundamental geomechanics equations are solved iteratively at all the nodes of an element size. For coupled diffusion-displacement problems in Abaqus Standard, care was taken when choosing the units of the problem for consistency. This is because the coupled equations may be numerically ill-conditioned if the choice of units are mixed thereby causing the output values generated by equations from two different fields to differ by many orders of magnitude. The International System of units (SI) were used for all Abaqus inputs in this study. In Abaqus, porous media is modeled approximately by attaching the finite element mesh to the solid phase such that fluid can flow through this mesh. The model uses a continuity equation for the mass of wetting fluid per unit volume of the medium and the mechanical part of this model is based on the effective stress principle. The finite element formulation details used in Abaqus can be found in the theory guide of the Abaqus user documentation (Version 6.14, SIMULIA 2014) and is available online using a valid license. Here, only a concise summary of the fundamental equations from the theory guide are discussed. Abaqus uses the engineering sign convention for stresses which identifies compressive stress as negative and tensile stress as positive. This sign convention is opposite of the geoscience sign convention used in CMG. According to the Abaqus documentation theory guide, the effective stress is given by the following general form:

$$\sigma' = \sigma + \left(\chi u_w + (1-\chi) u_a\right) I \tag{33}$$

Where χ represents the saturation of the system, u_w is the average pressure stress in the wetting liquid, and u_a is the average pressure stress in the other non-wetting fluid (for unsaturated cases). For a fully saturated system, $\chi = 1$ and assuming that u_a is negligible, the above effective stress becomes:

$$\sigma' = \sigma + u_w I \tag{34}$$

The above expression is similar to the Terzaghi effective stress definition used in CMG with the exception of the sign convention. In Abaqus compressive stress is negative while in CMG compressive stress is positive. Input parameters used in the Abaqus for modeling coupled fluid flow with stress in poroelastic media include: mass density, bulk modulus of fluid and solid grain, hydraulic conductivity, void ratio, logarithmic bulk modulus, poisson’s ratio, specific weight of the wetting liquid, and flow rate among others. The void ratio (e) is defined as a function of porosity (ϕ):

$$e = \frac{\phi}{1-\phi} \tag{35}$$

In the Abaqus documentation theory guide, the elastic portion of the volume ratio between the reference and current state (J^{el}) is defined as follows:

$$J^{el} = \frac{\kappa}{1+e_i} \ln\left(\frac{\sigma_{mi} + \sigma_t^{el}}{\sigma_m + \sigma_t^{el}}\right) + 1 \tag{36}$$

Where e_i is the initial void ratio, σ_t^{el} is the elastic tensile stress limit, $\sigma_m$and σ_{m_i} are the mean and initial mean stresses and κ is the logarithmic bulk modulus. Assuming $\sigma_t^{el} \gg \sigma_{m_i}$ and $\sigma_t^{el} \gg \sigma_m$, the logarithmic bulk modulus is given by:

$$\kappa = \frac{1+e_i}{K_d}\left(\sigma_m + \sigma_t^{el}\right) \tag{37}$$

Where K_d is the drained bulk modulus is expressed as a function of the Young's modulus and the passion ratio:

$$K_d = \frac{E}{3(1-2v)} \tag{38}$$

The shear modulus (G) can be expressed as a function of drained modulus or Young modulus as follows:

$$G = K_d \frac{3(1-2v)}{2(1+v)} = \frac{E}{2(1+v)} \tag{39}$$

The discretized equilibrium statement for a porous medium is defined in Abaqus by the principle of virtual work for the volume under consideration in its current configuration at a given time. The upper case superscript notation,N, in the equations below signifies the discretization of for the finite element model approximated by interpolation functions $\left(\vec{\mathrm{N}}^N, \beta^N\right)$ using the Lagrangian framework.

$$\begin{gathered}\int_V \vec{\sigma} : \delta\vec{\varepsilon}\, dV = \delta\vec{\mathrm{v}}\left[\int_S \vec{t}\; dS + \int_V \vec{f} dV + \int_V \left[n_f \gamma_w\right] dV\right] \\ \delta\vec{\mathrm{v}} = \vec{\mathrm{N}}^N \delta\mathrm{v}^N \\ \delta\vec{\varepsilon} = \beta^N \delta\mathrm{v}^N = sym\left(\frac{\partial\delta\vec{\mathrm{N}}^N}{\partial\vec{\mathrm{x}}}\right)\end{gathered} \tag{40}$$

Where γ_w is the specific gravity of the wetting fluid, $\vec{\sigma}$ is the Cauchy stress tensor, $\vec{t}$ are the surface tractions tensor per unit area, n_f is the total volume of wetting fluid (free plus trapped) per unit volume in the current configuration, $\vec{f}$ is the body force per unit volume (V) while $\delta\vec{\mathrm{V}}$ and $\delta\vec{\varepsilon}$ are respectively the virtual velocity field and the virtual rate of deformation both of which are a function of the Lagrangian framework interpolation functions $\left(\vec{\mathrm{N}}^N, \beta^N\right)$. The virtual work principle with assumed independent incremental virtual velocity field, $\delta\mathrm{V}$, can then be expressed more familiarly as a balance between internal and external acting force arrays such that the virtual velocity field cancels out as seen below:

$$\begin{gathered}\delta\mathrm{v}\int_V \vec{\sigma} : \delta\vec{\varepsilon}\, dV = \delta\mathrm{v}\left[\int_S \vec{t}\; dS + \int_V \vec{f} dV + \int_V \left[n_f \gamma_w\right] dV\right] \\ \delta\mathrm{v}^N \int_V \vec{\sigma} : \vec{\beta}^N dV = \delta\mathrm{v}^N N^N \left[\int_S \vec{t} dS + \int_V \vec{f} dV + \int_V \left[n_f \gamma_w\right] dV\right] \\ \delta\mathrm{v}^N I^N = \delta\mathrm{v}^N P^N \\ I^N + \left(-P^N\right) = 0\end{gathered} \tag{41}$$

The continuity equation, required to equate the rate of increase of in the fluid mass stored at a node to the rate of mass of fluid flowing into the node within a given time increment, is integrated in time using the backward Euler approximation. This equation is satisfied approximately in the finite element model by using excess wetting liquid pressure (P_w) as the nodal variable interpolated over the elements. The total derivative of the integrated variational form of the continuity statement with respect to the nodal variables is required for the newton iterations employed for solving non-linear, coupled, equilibrium equations. For a relatively incompressible wetting liquid in a porous medium, the continuity equation in terms of the finite element approximation variational form equates the time rate of change of a given mass of wetting fluid to the addition of fluid mass across the surface.

$$\int_V \frac{1}{J}\frac{d}{dt}\left(J\,\rho_w\left(n_w+n_t\right)\right)dV=-\int_S\left(\rho_w n_w \vec{n}\cdot\overrightarrow{V_w}\right)dS \tag{42}$$

The nodal continuity statement by virtue of the divergence theorem for an arbitrary volume, can be written as:

$$\frac{1}{J}\frac{d}{dt}\left(J\,\rho_w\left(n_w+n_t\right)\right)+\frac{\partial}{\partial\vec{x}}\left(\rho_w n_w\overrightarrow{V_w}\right)=0 \tag{43}$$

Where $\overrightarrow{V_w}$ is the average velocity of the wetting fluid relative to the solid phase (seepage velocity), J is the ratio of the fluid volume in the current configuration to the fluid volume in the reference configuration, $\vec{n}$ is the outward normal to the surface (S), ρ_w is the density of the wetting fluid, n_w and n_t are the volume ratio of free wetting fluid and the volume ratio of trapped fluid at a point. Rewriting the above expression in the weak form, and employing an arbitrary continuous wetting fluid pore pressure variational field test function (δP_w), Abaqus solves the continuity statement normalized with the wetting fluid density at a reference state $\left(\rho_w^i\right)$ by integrating approximately in time using the backward Euler formula:

$$\int_V \left[\delta P_w \left(\frac{\rho_w}{\rho_w^i} \left(n_w + n_t \right) \right) - \frac{1}{J} \left(\frac{\rho_w}{\rho_w^i} J \left(n_w + n_t \right) \right)_t - \Delta t \frac{\rho_w}{\rho_w^i} n_w \frac{\partial \delta P_w}{\partial \vec{x}} \overrightarrow{V_w} \right] dV$$

$$+\Delta t \int_S \delta P_w \left(\frac{\rho_w}{\rho_w^i} n_w \vec{n} \cdot \overrightarrow{V_w} \right) dS = 0 \tag{44}$$

The discretized equilibrium equations together with the continuity formulation for a wetting fluid in a porous media described above both define the state of the porous medium (Abaqus 2014 guide).

The constitutive behavior of the pore fluid flow is governed by Darcy’s law which is considered a linearized version of Forchheimer’s law for fluid flow at low velocity. Permeability in Abaqus Standard Analysis is defined from the relationship between porous media volumetric flow rate per unit area of a particular wetting fluid and the gradient of the effective fluid pressure. For a coupled pore fluid diffusion and stress analysis, Abaqus defines the permeability in general as a function of fluid flow velocity according to Forchheimer’s law. According to Forchheimer’s law, high flow velocities can reduce the effective permeability and lead to a choked pore fluid flow. At low fluid flow velocities, Forchheimer’s law becomes a good approximation of the well-known aforementioned Darcy flow. For pore fluid flow, Forchheimer’s law can be written as follows:

$$\vec{\dot{Q}} \left(1 + \beta \sqrt{\overrightarrow{V_w} . \overrightarrow{V_w}} \right) = -\frac{k_s}{\gamma_w} k . \left(\frac{\partial P_w}{\partial \vec{x}} - \gamma_w \right) \tag{45}$$

Where $\overrightarrow{\dot{Q}}$ is the volumetric flow rate per unit area of a particular wetting fluid, $\overrightarrow{V_w}$ is the fluid velocity, β is a velocity coefficient, k and k_s are the permeability of a fully saturated medium and dependence of permeability on the saturation of the wetting fluid $(k_s|_{s=1} = 1)$, while P_w and γ_w are the wetting fluid pore pressure in spatial coordinate $\vec{x}$ and specific weight respectively. The permeability in this study is isotropic and can be given as a function of void ratio. The hydraulic conductivity- permeability relationship is defined in general as:

$$\text{Ҡ} = \frac{k_s}{\left(1 + \beta\sqrt{\overrightarrow{V_w}.\overrightarrow{V_w}}\right)} k \tag{46}$$

For Darcy flow at low velocities, the velocity coefficient is approximately zero. The general Forchheimer's law can be re-written in terms of the hydraulic conductivity as follows:

$$\vec{\dot{Q}} = -\frac{\text{Ҡ}}{\gamma_w}\left(\frac{\partial P_w}{\partial \vec{x}} - \gamma_w\right) \tag{47}$$

For soils consolidation problems like the one in this study, the fully saturated permeability is given as a function of void ratio. Comparing the above Forchheimer expression at low pore fluid flow velocities in relation to the Darcy Law, a simplified expression for the hydraulic conductivity-permeability relationship can be obtained. The hydraulic conductivity (Ҡ), the term through which permeability is defined in Abaqus, is then defined as a function of permeability (k).

$$\text{Ҡ} = \frac{\gamma_w\, k}{\mu} = \frac{\rho_w g\, k}{\mu} \tag{48}$$

Where $\gamma_w$and ρ_w is the specific weight and density of the wetting fluid, μ is the fluid viscosity, g is the gravitational constant while k is the permeability of the rock. A Steady state analysis method using the "soils" keyword is used for the coupled pore pressure effective stress analysis. This assumes that there are no transient effects in the wetting liquid equation because the steady state solution corresponds to constant wetting liquid velocities and constant volume of the wetting fluid per unit volume of the continuum. Pore fluid flow in Abaqus is prescribed as a node-based seepage flow directly in consolidation analysis using the "cflow" keyword to apply a concentrated fluid flow at the node. Combining the force equilibrium, constitutive relationship, kinematic strain displacement yields the geomechanics solution solved in Abaqus using the finite element method and in CMG using finite difference method. Abaqus uses a stabilized finite element iteratively coupled model which when converges yields the same result as a fully coupled model. However in CMG, which uses the finite difference method, these equations are solved only at the center of an element of the same size. A stabilized iteratively coupled fluid flow with geomechanics model when converged is in some cases analogous to a fully coupled model approach. Pore pressure, stress variations and strain changes are compared between a finite element method model in Abaqus and a finite difference method model in CMG. The resulting seismic moment magnitudes are calculated from both models and compared. Further coupling details in CMG versus Abaqus are beyond the scope of the thesis. However, more details can be found in the Denney (2006) and Abaqus 2014 manual respectively in the references.

2.3 Abaqus and CMG Comparison

The Abaqus and CMG simplified test models in this study are developed towards eventually achieving a practical Azle field case study with a similar reservoir grid structure and geomechanical setup (Hornbach et al., 2015). The two dimensional test models currently assume one injection and one production well evenly spaced in the target formation. A $62 \times 1 \times 22$ centered Cartesian grid with uniform single block in the y direction is used to represent $10 \times 10 \times 10\ Km$ formation with five layers. The six formation zones from top to bottom, each with different geomechanical properties, are the Overburden, reservoir layers "A", "B", and target zone "C", as well as Upper and Lower Basements. The models assume single phase fluid flow in and out of the target formation referred to as "C". A vertically staggered fault geometry is used in the model. The basement formation is the zone of interest for investigating strain change. Table 2 below summarizes the general properties of the test models developed. Fig. 6 and Fig. 7 respectively illustrate the overall CMG and Abaqus models (not shown to scale).

Table 2 – General Reservoir Test Model Summary

Fluid Flow	Size (x, y, z) $[km]$	$10x10x8$
	Center Grid Dimension	N_x=62 ; N_y=1 ; N_z=22
	6 Zones (Top-Down)	Overburden, Reservoir Layers ["A", "B", and target zone "C"], Upper and Lower Basements
	Flow system	Single Phase
	Reservoir properties (k,ϕ..)	Global Heterogeneous (Homogeneous by zone)
	Production	Two Unbalanced injector/Producer in "C"
Geomechanics	Failure criteria	Staggered vertical Fault
	Fault	Mohr-Coulomb
	Seismic moment magnitude	In- house codes

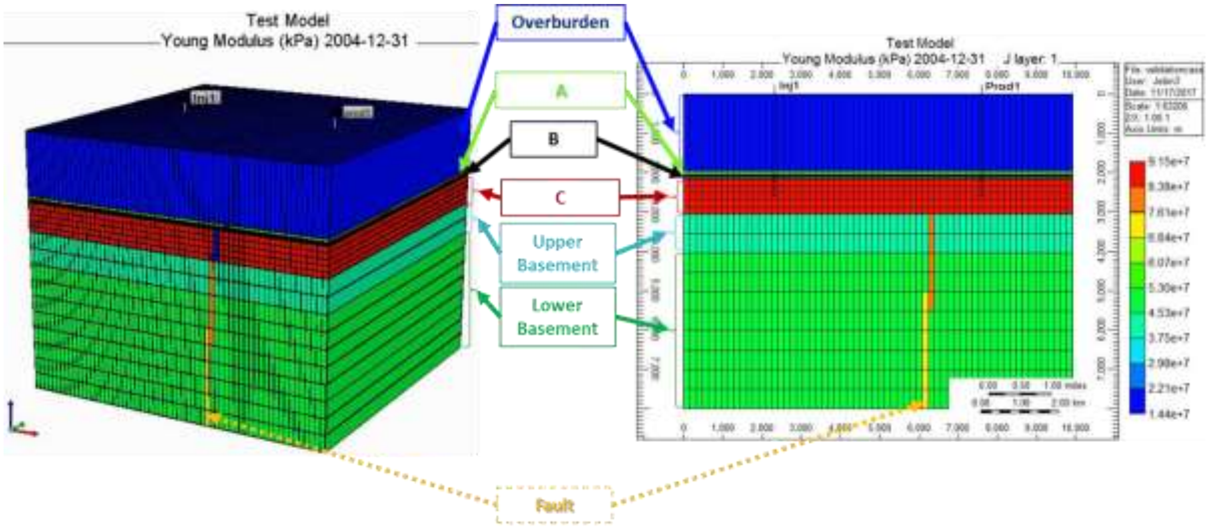

Fig. 6 – CMG Test Model with 3D View (Left) and Vertical Cross Section View (Right)

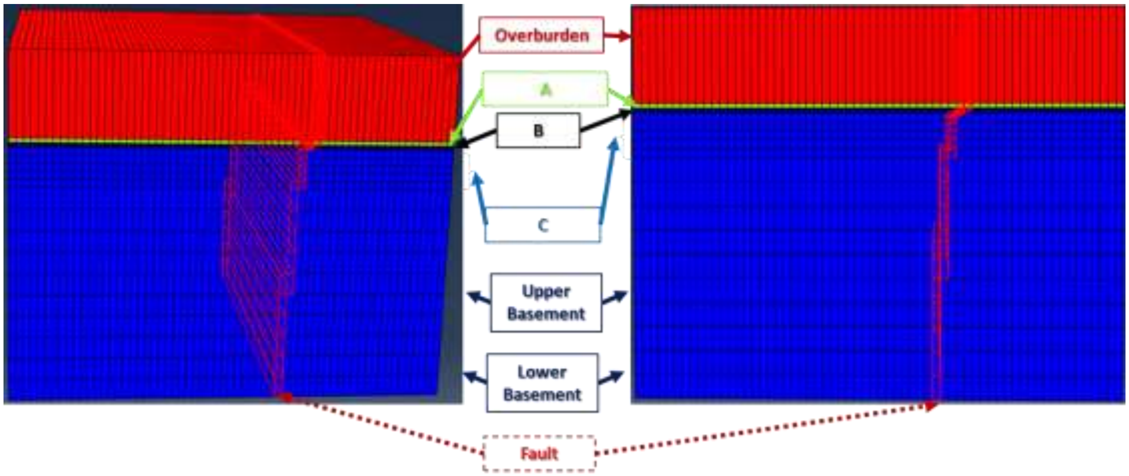

Fig. 7 – Abaqus Test Model With 3D View (Left) and Vertical Cross Section View (Right)

For a simple homogenous case, the following geomechanical inputs were provided to both Abaqus and CMG models as shown in Table 3 below. This setup is for a scenario where much of the fluid flow is constrained within the target "C" formation with constant properties across formation zones and within the staggered fault. Reservoir properties for the test models were adapted from

(Hornbach et al., 2015) and Texas Rail Road Commission database (TRC 2015a, 2015b) while geomechanical properties were adapted from (Snee and Zoback 2016) and (Wang 2000).

Table 3 – Geomechanical Inputs for Case Study

	Overburden	“A”	“B”	“C”	Basement	Fault	Reference
Permeability (md)	0	0	0	30	0	0	Simplified Hornbach et al. 2015; TRC 2015a; TRC 2015b;
Porosity	0.055	0.055	0.055	0.05	0.055	0.05	
Pore Pressure	11.2 kPa/m						Test Model
Vertical Effective Stress	14.5 kPa/m						Test Model
Minimum Effective Horizontal Stress	4.5 kPa/m						
$A_\phi = (s2 - s3)/(s1 - s3)$	0.27						
Direction of Horizontal Stress	N26.2E						
Young’s Modulus (kPa)	6e7	6.0e7	6e7	6e7	6e7	2e7	Adapted from Wang 2000
Poisson’s Ratio	0.2	0.2	0.2	0.2	0.2	0.2	
Cohesion (kPa)	2.0e4	2.0e4	2.0e4	2.0e4	2.0e4	1.5e3	
Friction Angle (Deg)	30	30	30	30	30	30	

Fig. 8 and Fig. 9 show the comparison on stress and strain output results between Abaqus and CMG (not shown to scale). It is important to note that compressive stress is negative in Abaqus but positive in CMG. As seen from the results, the stress distribution are similar and are of the same order of magnitude.

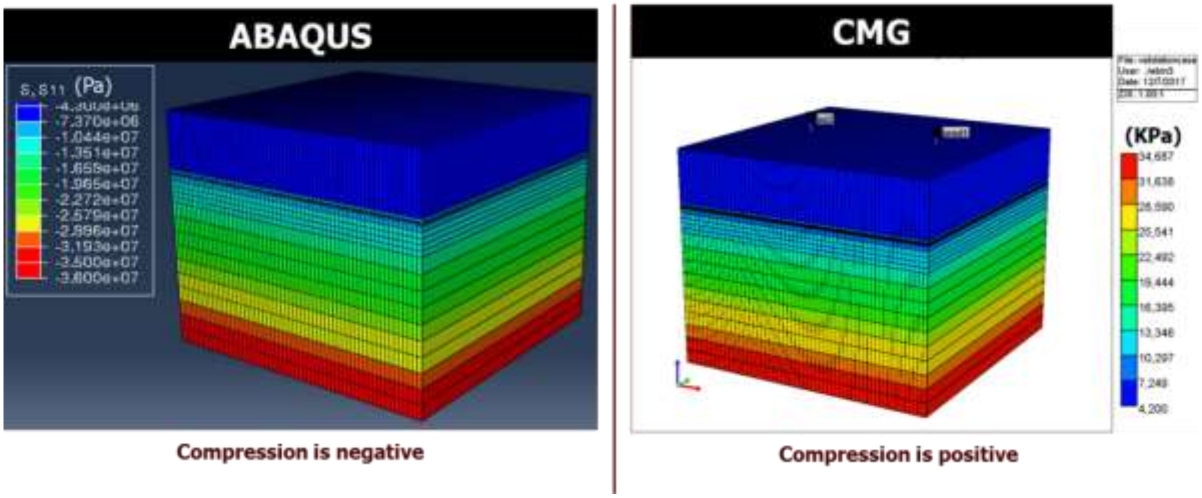

Fig. 8 – Compressive Normal Stress (Abaqus vs CMG)

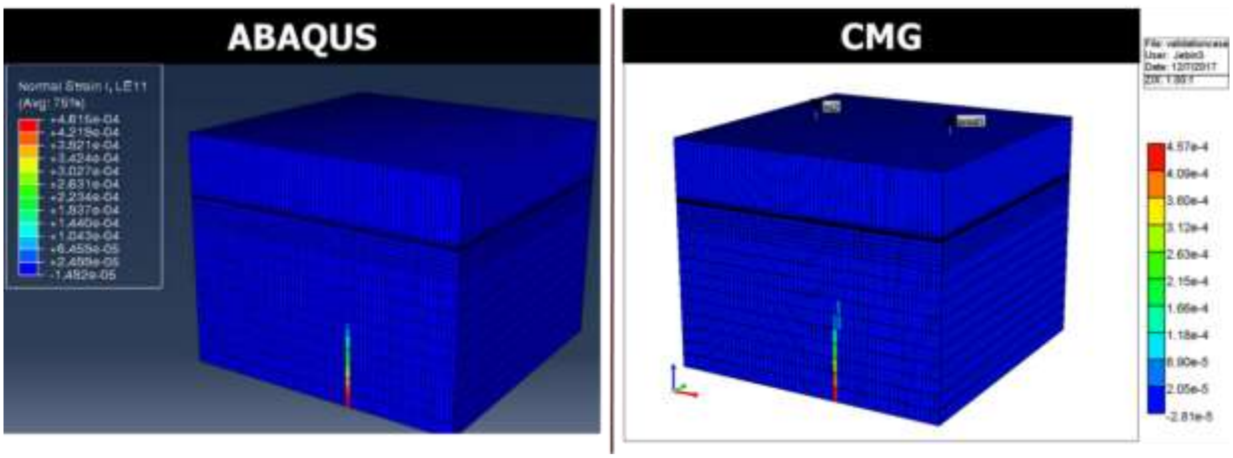

Fig. 9 – Normal Strain (Abaqus vs CMG)

Although the strains are of the same of order of magnitude between Abaqus and CMG and suggests an agreement between Abaqus and CMG, there is a slight difference in the normal strain output from both models due to differences in the numerical methods between the two commercial applications. Abaqus computes the strain values at nodes representing an element using the finite element method (nodal-based output) while CMG computes the strain value at the center of an element using the finite difference method (volume-based output). In this study, the nodal values for an element in Abaqus are averaged to yield a single value for the element via post processing codes in order to have a fair (apples to apples) comparison.

The basement strain change, target zone average pressure in fault vicinity and basement induced seismic moments are compared for a given balanced versus unbalanced scenario. Fig. 10 shows the results comparing the balanced versus unbalanced scenario. The term unbalanced in this study refers to any scenario where the fluid production rate is greater than the injection rate and when the pore volumes on either side of the fault are unequal. For the unbalanced case here, the production rate $\left(833.34\,\frac{m^3}{day}\right)$ is twice the injection rate $\left(416.67\,\frac{m^3}{day}\right)$ and there are more pore volumes on the left-hand injector side of the fault compared to the right-hand producer side of the fault. For the balanced case, the production and injection rates are equal $\left(416.67\,\frac{m^3}{day}\right)$ while the pore volumes on either side of the fault are also equal. The fault permeability $(3e^{-3}\ md\ )$ is four orders of magnitude less than the target zone permeability$(30\ md\ )$ to signify a barrier to flow. The blue lines indicate the balanced case results while the orange lines indicate the unbalanced case results. Results show that there is more pressure decline, increase in strain change and increase in seismic moments for unbalanced production-injection activity. As suggested by the results, unbalanced conditions lead to more strain change and induced seismicity.

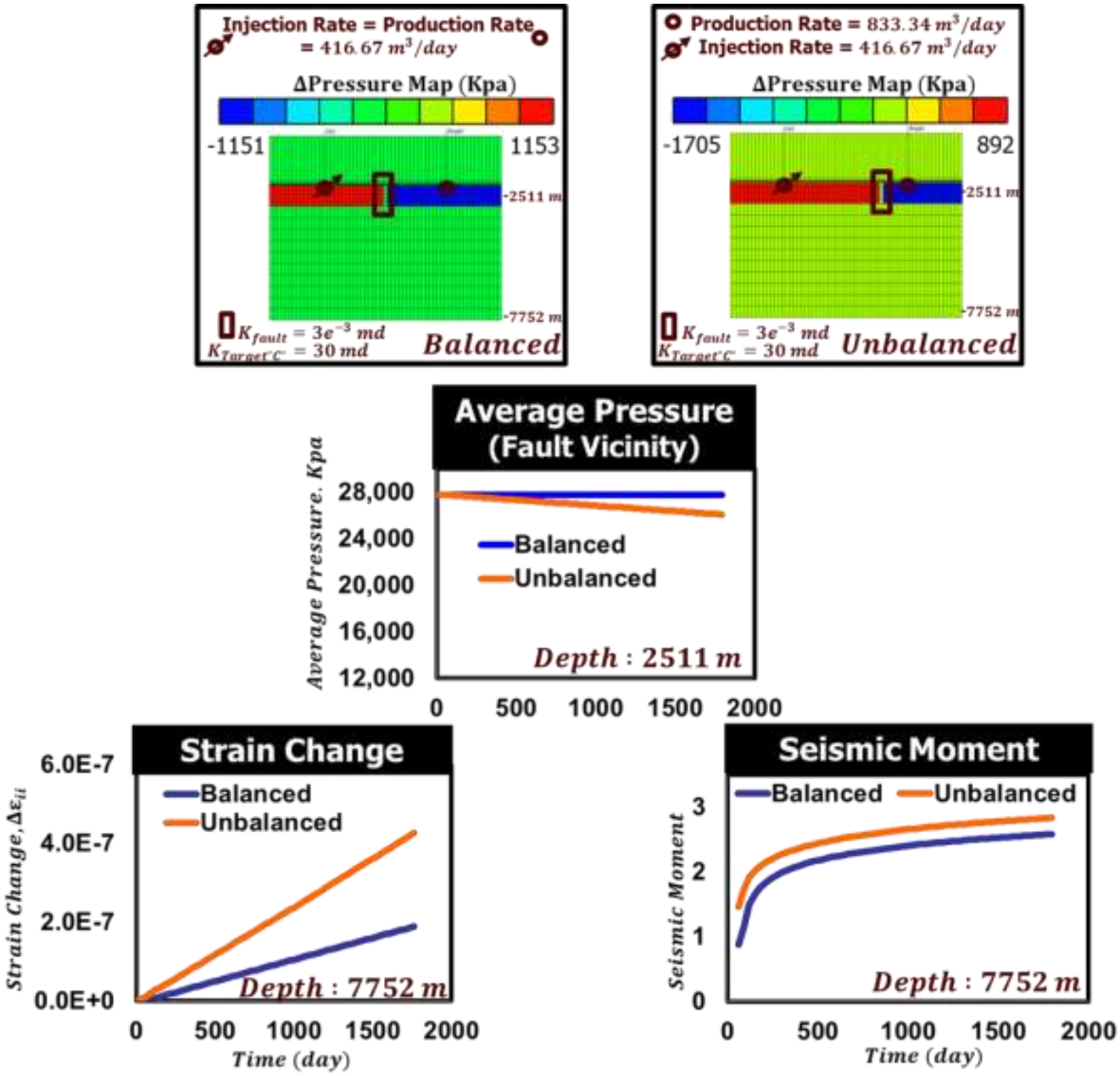

Fig. 10 – Balanced vs Unbalanced Scenario

CHAPTER III

UNBALANCED LOADING CASE STUDY

3.1 Unbalanced Case Study

An unbalanced waste water injection well and brine production well case study in a reservoir system with underlying fault is examined using test models to observe the strain change using both finite element and finite difference methods. Fig. 11 below shows the strain change over a time frame of 300 days at the middle $(5771\ m)$, and bottom $(7752\ m)$ portions of the basement using in Abaqus and CMG. The producing well operated at a rate of $800\,\frac{m^3}{day}$ while the injection well operated at a rate of $400\,\frac{m^3}{day}$.

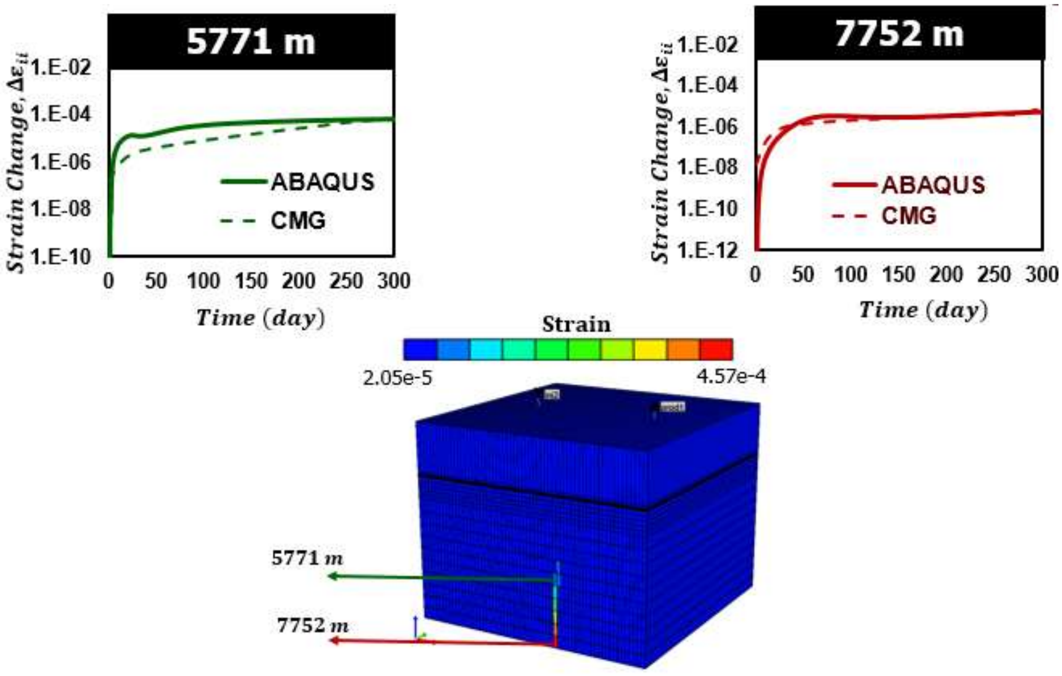

Fig. 11 – Strain Change Comparison due to Unbalanced Loading (Abaqus vs CMG)

Overall, a similar trend is observed in strain change between Abaqus and CMG. However, CMG absolute strain change results slightly differ and under estimate the strain change results from Abaqus. This slight discrepancy is suggested to be due to differences in the discretization because the finite element approach in Abaqus solves the equilibrium and fluid flow system of equations simultaneously at all the nodes of a given element whereas finite difference approach in CMG sequentially solve these equilibrium and fluid flow equations as an average over the given element. According to Wang (2000), poroelastic coupling in the finite element framework can produce non-monotonic pore pressure behavior following undrained loading and this can affect strain change especially at early times. A stress free boundary indicates that poroelastic stresses are due to non-linear pore pressure distribution effects for the classic example of the hydrostatic loading of a rectangular plate. This non-monotonic pore pressure behavior due to poroelastic coupling is known as the Mandel-Cryer phenomenon described in chapter four. It is important to note that during simulation period, initial instabilities in the iteratively coupled method in Abaqus can yield a non-smooth strain response at early times. Results suggest that unbalanced injection-production activity in the target formation can lead to increased strain change and induced seismicity in the reservoir basement due to pore pressure change. In the next section, a sensitivity study is conducted in CMG to examine the effect of various production and injection flow patterns on the strain change before more unbalanced case studies are compared between Abaqus and CMG.

3.2 Strain Change Response to Flow Patterns

The strain change output in the reservoir basement is compared for different scenarios of varying production-injection rate flow patterns over a five year period. The volumes for cumulative production and cumulative injection over the total simulated time period are $1.5 \times 10^6\ m^3$ and $7.5 \times 10^5\ m^3$ respectively. Table 4 summarizes all five different production-injection pattern scenarios. Beginning from a base case constant production rate and constant injection rate, the production or injection rates are linearly increased or decreased while the other rate is held constant.

Table 4 – Varying Production-Injection Pattern Scenario Summary

	Scenario 1	**Scenario 2**	**Scenario 3**	**Scenario 4**	**Scenario 5**
Injection Pattern	Constant	Constant	Constant	Linearly increasing	Linearly decreasing
Production Pattern	Constant	Linearly increasing	Linearly decreasing	Constant	Constant

Fig. 12 through Fig. 16 illustrate the corresponding flow rate and cumulative volume progression for each of the five scenarios. The production rates and cumulative production volumes are indicated in blue while the injection rates and cumulative injection volumes are indicated in red. For each of these scenarios, the basement strain change as a result of the activity in the target, “C”, formation is observed over a period of over five years.

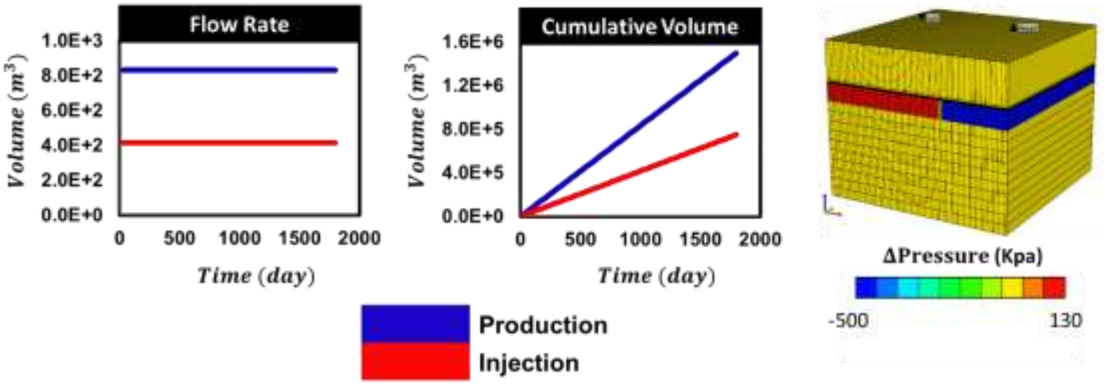

Fig. 12 – Scenario 1 (Constant Production and Injection Rates)

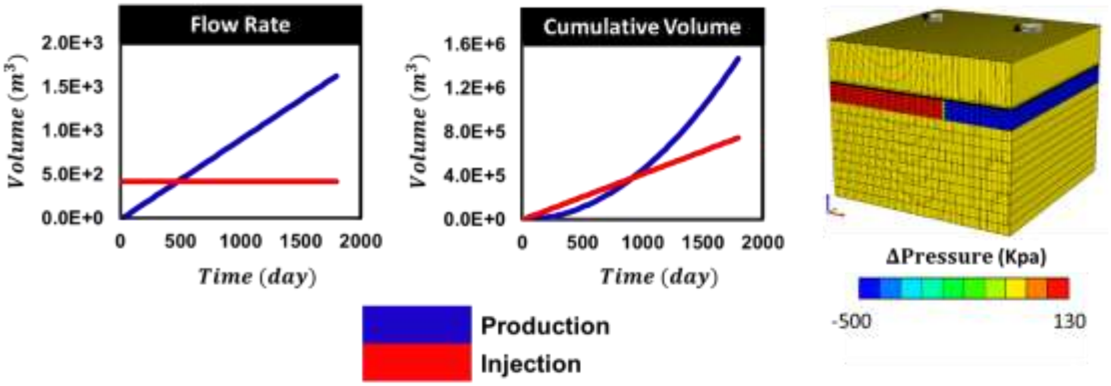

Fig. 13 – Scenario 2 (Increasing Production and Constant Injection Rates)

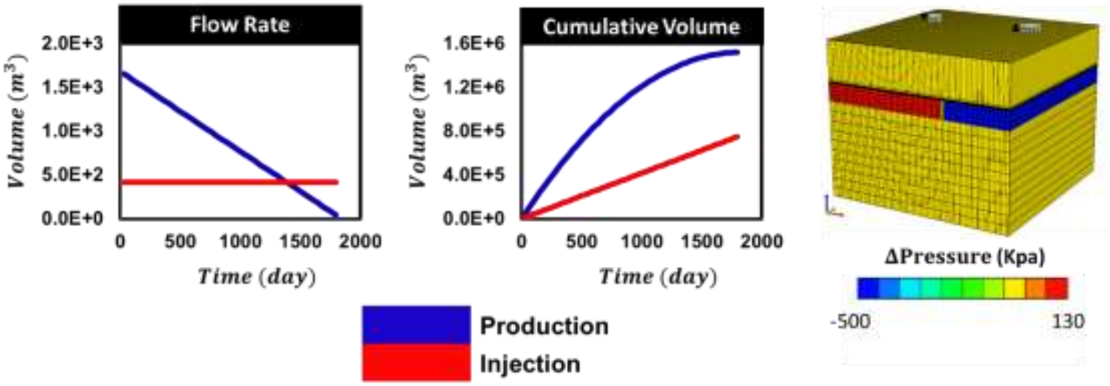

Fig. 14 – Scenario 3 (Decreasing Production and Constant Injection Rates)

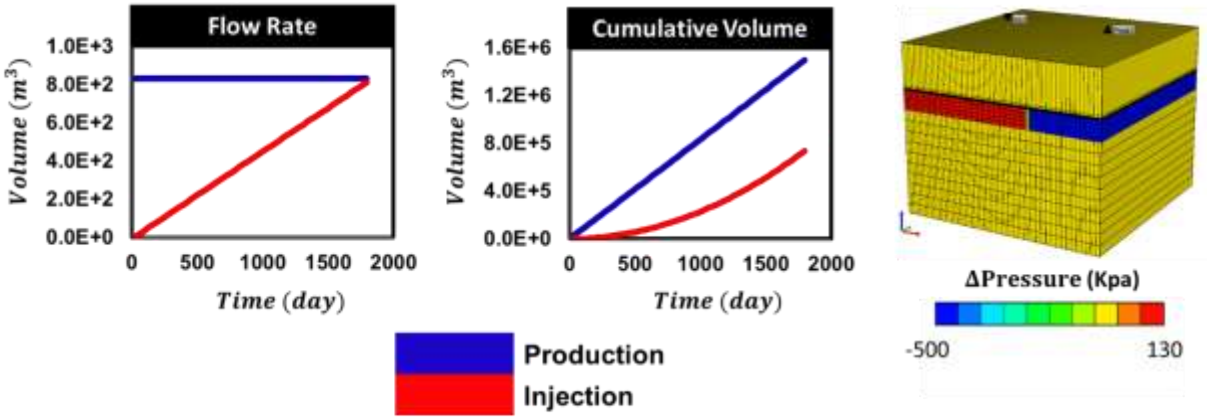

Fig. 15 – Scenario 4 (Constant Production and Increasing Injection Rates)

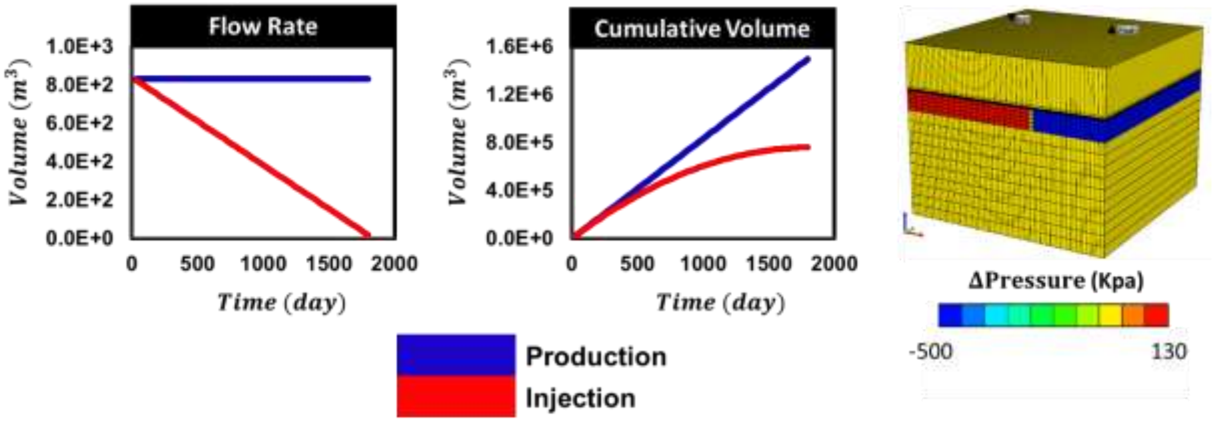

Fig. 16 – Scenario 5 (Constant Production and Decreasing Injection Rates)

In scenario 1 (base case), the production and injection rates are held at a constant rate $800 \frac{m^3}{day}$ of and $400 \frac{m^3}{day}$ respectively. In scenario 2, the injection rate is held constant at $400 \frac{m^3}{day}$ while the production rate is linearly increased from $13.888 \frac{m^3}{day}$ to a maximum of $1.625 \times 10^3 \frac{m^3}{day}$ over the five year timeframe. In scenario 3, the production rate is held constant at $800 \frac{m^3}{day}$ while the injection rate is linearly decreasing from a maximum of $1.625 \times 10^3 \frac{m^3}{day}$ to a minimum of $41.666 \frac{m^3}{day}$ over the five year timeframe. In scenario 4, the production rate is held constant at $400 \frac{m^3}{day}$ while the injection rate is linearly increasing from a minimum of $6.944 \frac{m^3}{day}$ to a maximum of $8.125 \times 10^2 \frac{m^3}{day}$ over the five year timeframe. In scenario 5, the production rate is held constant at $800 \frac{m^3}{day}$ while the injection rate is linearly decreasing from a maximum of $8.125 \times 10^2 \frac{m^3}{day}$ to a minimum of $20.833 \frac{m^3}{day}$ over the five year timeframe. For each of these scenarios, the strain change response relative to the base case is observed for scenarios 2 and 3 in Fig. 17 and for scenarios 4 and 5 in Fig. 18 below:

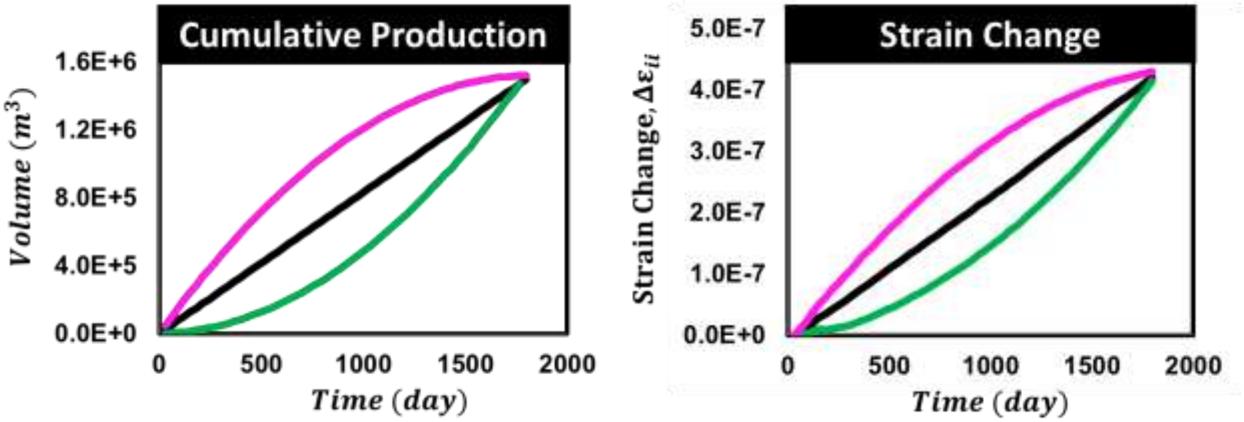

Fig. 17 – **Strain Change Comparison (Varying Production Rates- Scenarios 2 and 3)**

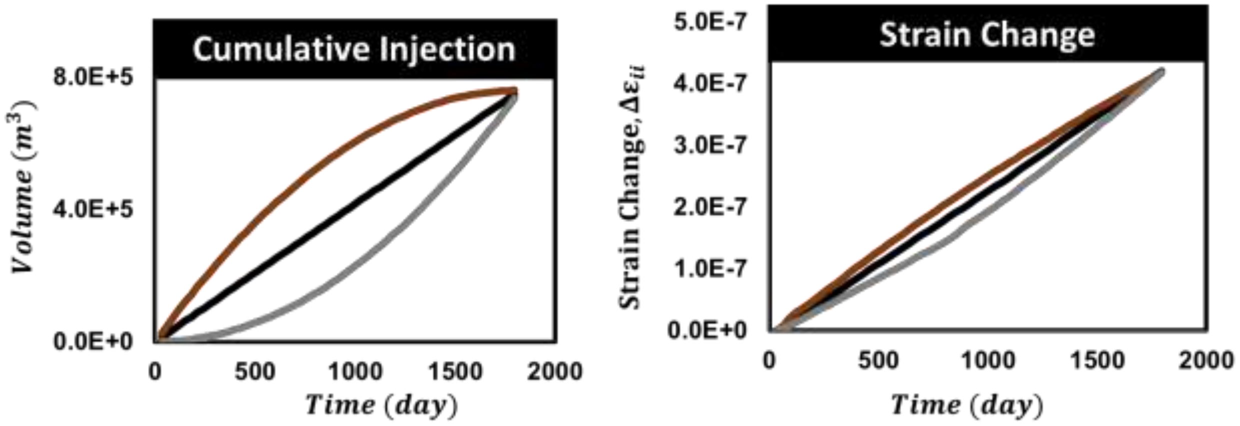

Fig. 18– Strain Change Comparison (Varying Injection- Scenarios 4 and 5)

The strain change follows a similar trend to the cumulative production volume for scenarios 2 and 3 where the production rate is linearly increased and decreased respectively with a constant injection rate. When the production rate is linearly increasing, the cumulative production volume and strain change follow a similar concave up trend as shown in green. On the other hand, when the production rate is linearly decreasing, the cumulative production volume and strain change follow a similar concave down trend over time as shown by the magenta curve. A similar trend applies for scenarios 4 and 5 where the injection rate is linearly increased and decreased respectively with a constant production rate. When the injection rate is linearly increasing, the cumulative injection volume and strain change follow a similar concave up trend as show in grey. On the other hand, when the injection rate is linearly decreasing, the cumulative injection volume and strain change follow a similar concave down trend shown in brown. However, the strain change due to varying injection rate is not as significant as compared to the strain change due to varying production rate. This suggests that the strain change in the basement near the fault zone is highly dependent on varying production pattern than injection pattern as a result of more compaction. The effect of production induced compaction is more pronounced because the fault is closer to the producer than the injector and more fluid is effectively produced than injected. The target formation region on the injection side has more pore volume than the target formation region on the production side. This explains why the strain change will be more dependent on the production pattern relative to the injection pattern.

3.3 Induced Seismicity

A fundamental parameter for describing the strength of earthquakes is the seismic moment which can range from the order of relatively small (10^{12}) to relatively large (10^{30}). Rutqvist et al., 2013 used the seismic moment tensor to model seismicity induced by fault activation. After the Mohr Coulomb failure criteria is satisfied, plasticity effects kick in pose elasticity. Using strain change from Geomechanics simulation results, cell volume and geomechanical properties, the seismic moment tensor can be determined. Fault activated induced seismicity can be defined using the seismic moment tensor,$\vec{M}_{pq}$, which is a function of the tangential stiffness tensor,C_{pqrs}, and strain change,$\Delta\epsilon_{rs}$, product summed over the Volume,V, of the fault zone of interest (Aki and Richards, 2002) as follows:

$$\vec{M}_{pq} = \int_{V} \vec{C}_{pqrs} . \Delta \grave{o}_{rs} \, dV \qquad (49)$$

The seismic moment intensity,M_o, is defined as the L_2 norm of the seismic moment tensor:

$$M_o = \vec{M}_{pq_{L2}} \qquad (50)$$

The Kanamori correlation (Kanamori 1977) is used to convert the seismic moment intensity,M_o into the dimensionless seismic moment magnitude,M_w which is more frequently used to report the magnitude of seismic activity.

$$M_w = \frac{logM_o - 16.1}{1.5} + 4.667 \qquad (51)$$

CHAPTER IV

SENSITIVITY ANALYSIS OF RESERVOIR AND GEOMECHANICAL PROPERTIES

4.1 Failure Criterion and Mechanics-Geomechanics Analogy

In this work, the yield criterion describing the fault slip and activation is the Mohr Coulomb failure criterion. The Mohr Coulomb criteria is selected as the failure criteria which indicates the onset of yielding in the rock material. This criteria describes the shear-normal stress relationship and the conditions that favor fault slip and fault activation. For this failure criterion, the failure envelop is defined by a straight line indicating the onset of yielding. The effective shear stress is defined by a linear function of angle of internal friction with the effective normal stress as the slope and the cohesion as the intercept. Fig. 19 shows a graphical representation of the Mohr Coulomb criterion using Mohr Circle.

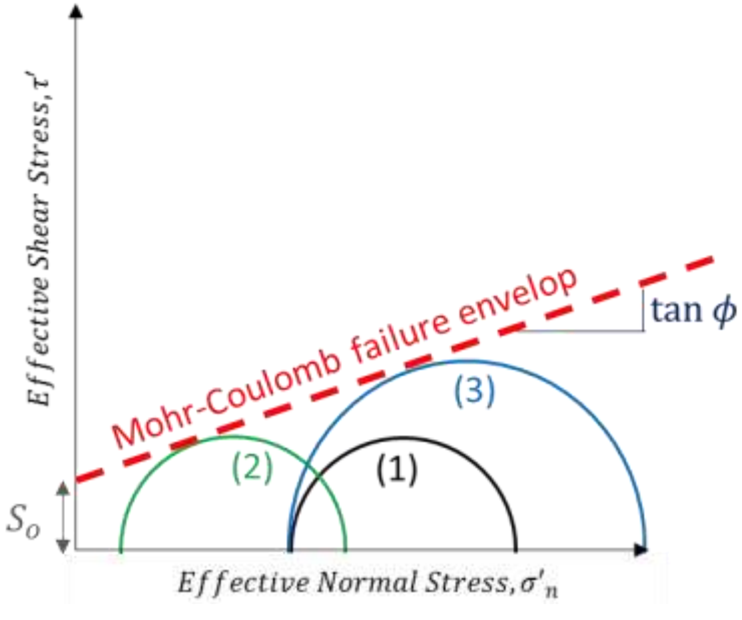

Fig. 19 – Mohr Coulomb Failure Criteria Illustration

The Mohr Coulomb envelope as defined by the red line is a linear expression of the effective shear stress (τ') as a function of the effective normal stress ($\sigma_n{}'$) such that S_o is the cohesion of the rock material and ϕ° is the angle of internal friction as follows:

$$\tau' = S_o + \sigma_n^{'} \tan\phi^{\circ} \tag{52}$$

The friction angle or angle of internal friction (ϕ°) is the maximum oblique angle between the normal and resultant stresses acting on a surface within a porous media. Typical values for the internal friction angle range from $30° - 45°$ and $\tan(\phi)$ ranges from $0.6 - 1.0$ (Zoback 2007, Reservoir Geomechanics). The rock material cohesion is usually described in the range of $0 - 6\ MPa$ (Fan et al., 2016; Rutqvist et al., 2013). The Mohr Circles (semi-circles) represent the stress state and defines the normal and shear stresses on a given 3D plane at a given instance. The minimum and maximum points where the semi-circles intersect the effective normal stress axis are respectively referred to as the minimum (σ_3) and maximum effective (σ_1) stresses. Shear failure occurs when the current stress state, which defines the normal and shear stress on a given plane, satisfies the linear Mohr-Coulomb failure envelop line shown in red. A graphical approach can be used to analyze fault slip and fault activation conditions. Given a particular stress state, fluid flow and geomechanical effects can be observed as the Mohr circle is displaced. For instance, given stress state 1, indicated by the black semi-circle in Fig. 19, if the pore pressure increases, the Mohr circle shift leftwards along the effective normal stress axis to the stress state 2, indicated by the green circle while maintaining the same radius. The increase in pore pressure leads to a decrease in the effective normal stress due to fluid flow effects. Also, if the effective maximum normal stress (σ_1) increases, more compression is observed in the rock and the stress state grows from state 1 to state 3, indicated by the blue circle, with increased circle radius. The increase in compaction occurs due to geomechanical effects. If the stress state at the fault is analogous to stress states 2 and 3 where the Mohr circle is substantially close to the failure envelop, the fault is said to be critically stressed.

In classical mechanics, consider the problem of a simple block on an inclined plane subjected to an applied load as shown below in Fig. 20. A free body diagram of the block illustrating all the external forces acting on it will include the applied load, body force (gravitational), and a frictional reaction force. Coulomb's friction law gives the frictional reaction force to be less than or equal to the product of the block's coefficient of friction $\left(\mu = tan\phi^{\circ}\right)$ relative to the inclined plane and the normal force $\left(\overrightarrow{f_N}\right)$ acting perpendicular to the block in contact with the inclined plane .

$$\overrightarrow{f_R} \leq \mu \times \overrightarrow{f_N} \tag{53}$$

For this simple mechanical system to maintain equilibrium, the downward force $\left(\overrightarrow{f_D}\right)$ should always be equal to the reaction force $\left(\overrightarrow{f_R}\right)$ along the inclined plane according to the principle of conservation.

$$\overrightarrow{f_D} = \overrightarrow{f_R} \tag{54}$$

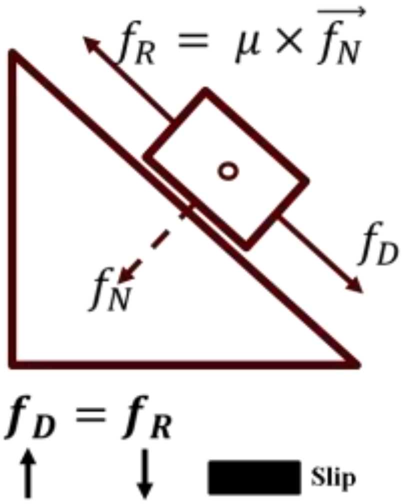

Fig. 20 – Classic Mechanics System

If the system is disturbed such that the normal force decreases, for a given constant downward force of the block along the inclined plane, then the frictional reaction force will decrease. When this reaction force declines below the constant downward force, the block will slide or slip down the inclined plane. We can say that a failure has occurred in the system.

Now consider a similar analog to geomechanics. The total overburden pressure (P_{OVB}) at a given depth is the summation of the fluid pressure (P_f) and the grain pressure (P_N) at that depth. The grain pressure and overbudden pressure from geomechanics can be considered respectively analogous to the normal force and downward force from classical geomechanics.

$$P_{OVB} = P_f + P_N \tag{55}$$

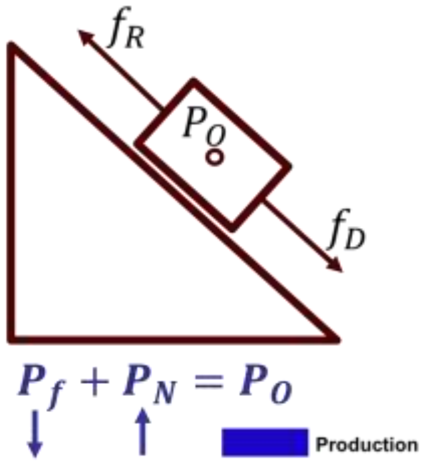

Fig. 21 – Geomechanics System Analogy

Consider the case where the overburden pressure is constant. If the fluid pressure at a given depth increases due to injection activity near a fault reservoir region, the normal expectation is that the grain pressure decreases to maintain equilibrium. As the grain pressure at the same given depth decreases, the friction with which the grains are held together reduces and slippage failure occurs in the system. However, if the fluid pressure decreases due to production activity as illustrated in Fig. 21, the grain pressure should increase to maintain equilibrium and there should be no slip. However, the above described scenario does not apply for the case of unbalanced production-injection activity considered in this study. It will be observed that as the fluid pressure decreases, due to more production activity, another factor at play can cause fault slip failure to occur which happens to be the strain change in this study.

4.2 Production-Injection Ratio Effect on Basement Strain Change and Induced Seismicity

The sensitivity of reservoir and geomechanical properties to strain change will be studied here. Previous work within the Texas A&M MCERI research group on a model similar to the Azle field case suggests that seismic events in the reservoir basement are not necessarily entirely caused by increase in pore pressure (Chen et al., 2018). The effect of change in the production to injection ratios on the basement strain at a depth of $7752\ m$ over a five year was investigated. The base injection rate was set at $416.67 \frac{m^3}{day}$ throughout the production-injection operations in the target "C" formation. For the base case, the production rate was set equal to the injection rate. The production rate was set to two times, five times and ten times the injection rate while the basement strain change and corresponding pore pressure changes were observed. Fig. 22 through Fig. 25 below show the basement strain change, induced seismicity and the corresponding pore pressure changes at the end of simulation as the ratio of production rate to injection rate was increased. As the rate of production to injection ratio was increased, more compaction occurred in the target "C" formation, and the strain change increased monotonically with a larger pore pressure difference at the end of the five year period. Although the fluid pressure continued to decline as the ratio of production to injection activity was increased, the induced seismic moment magnitude continued to increase (indicating more likelihood of fault slip failure) due to increasing strain change. The larger pressure change in the case of ratios 5 and 10 is because the stress change is too large due to exaggeration of the ratio of rates for a quasistatic geomechanic model simulation in CMG. The average pressure decline and effective normal stress increase in the base case where the production and injection rate are equal occur as a result of the placement of the fault barrier which has a much smaller permeability relative to the entire target “C” formation. The pore volumes on both sides of the fault are different. The injection region (left) of the fault has more pore volume than the production region (right) of the fault within the target formation. On average within the target formation, the pressure decrease due to production from a relatively small pore volume should be more than the pressure increase due to injection into a relatively large pore volume. Hence, more pressure drop will be observed near the fault on average even for the same production and injection rates applied in the base case. A view of the pore pressure map within the target formation shown in Fig. 22 confirms the reason for the average pressure decline in the base case.

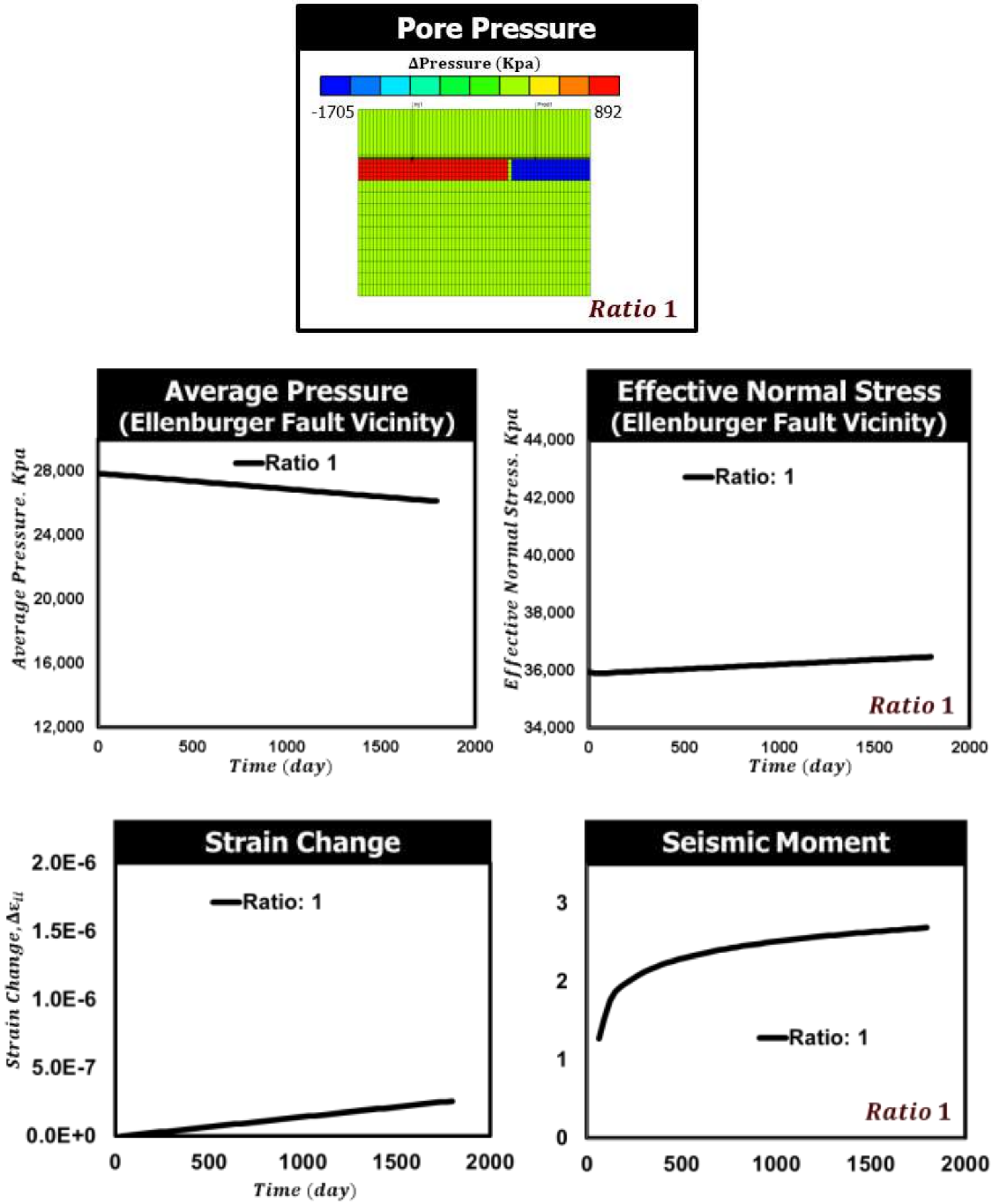

Fig. 22 – Basement Strain Change, Induced Seismicity, Stress, and Pressure for Ratio:1

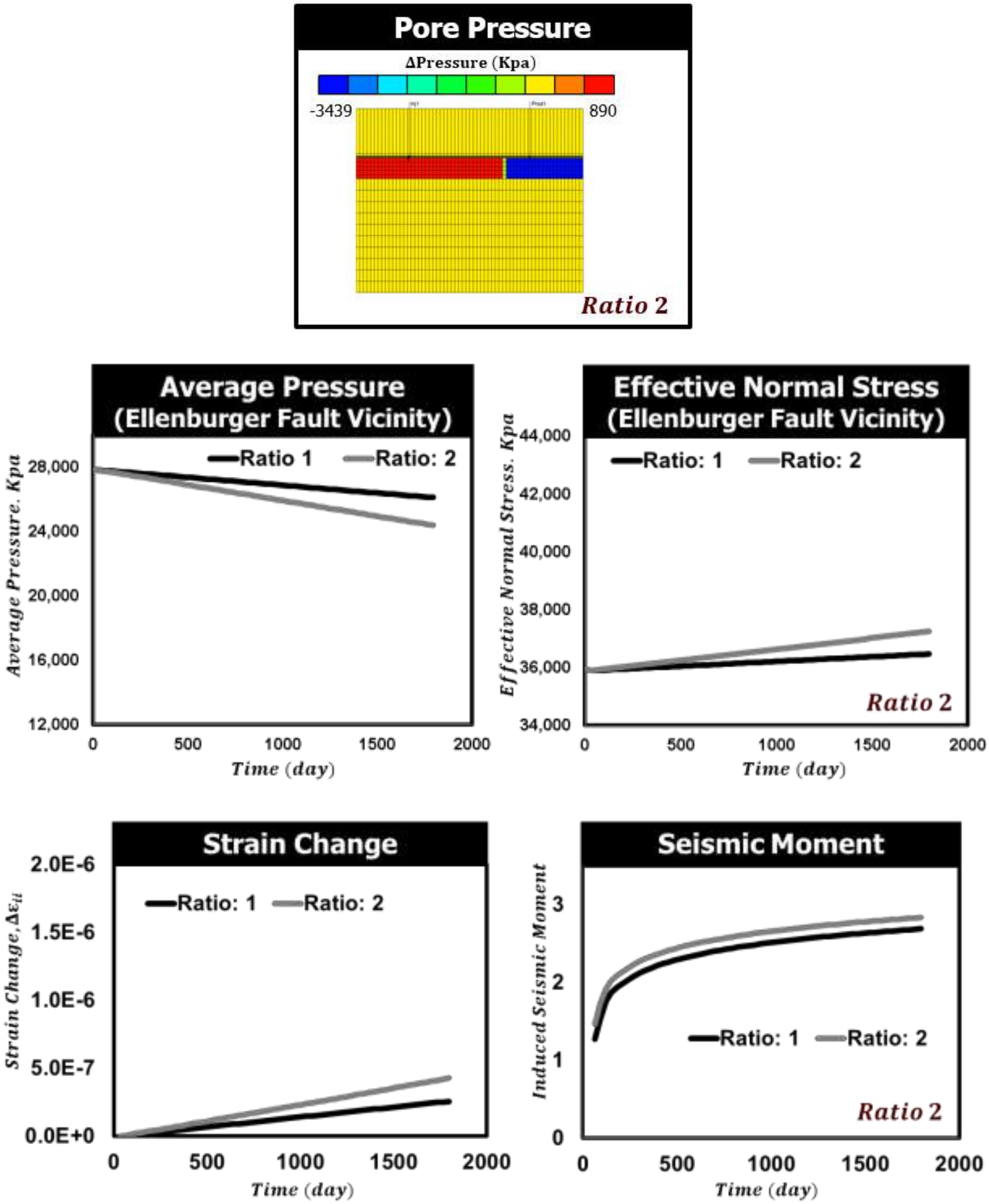

Fig. 23– Basement Strain Change, Induced Seismicity, Stress, and Pressure for Ratio: 2

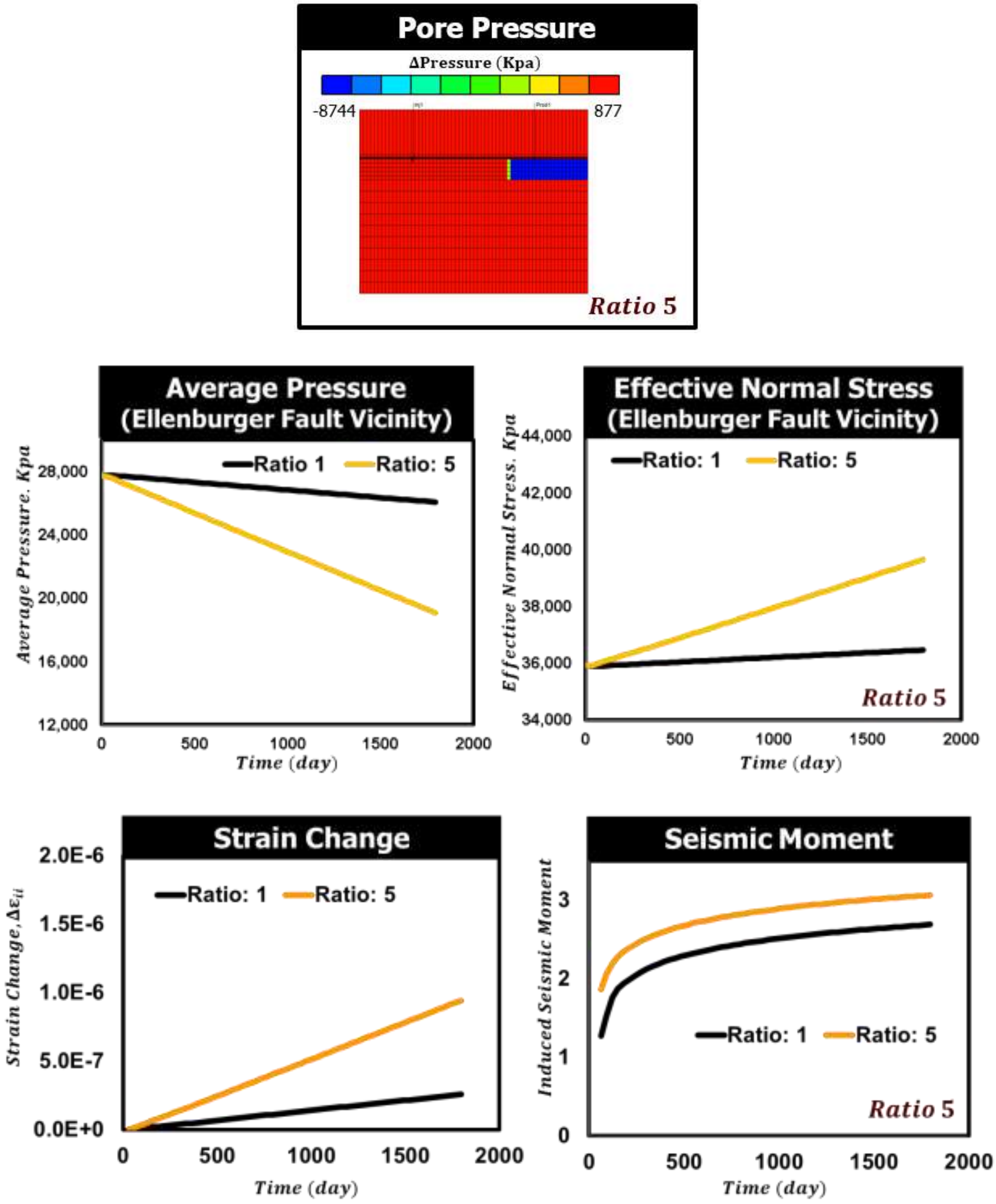

Fig. 24 – Basement Strain Change, Induced Seismicity, Stress, and Pressure for Ratio: 5

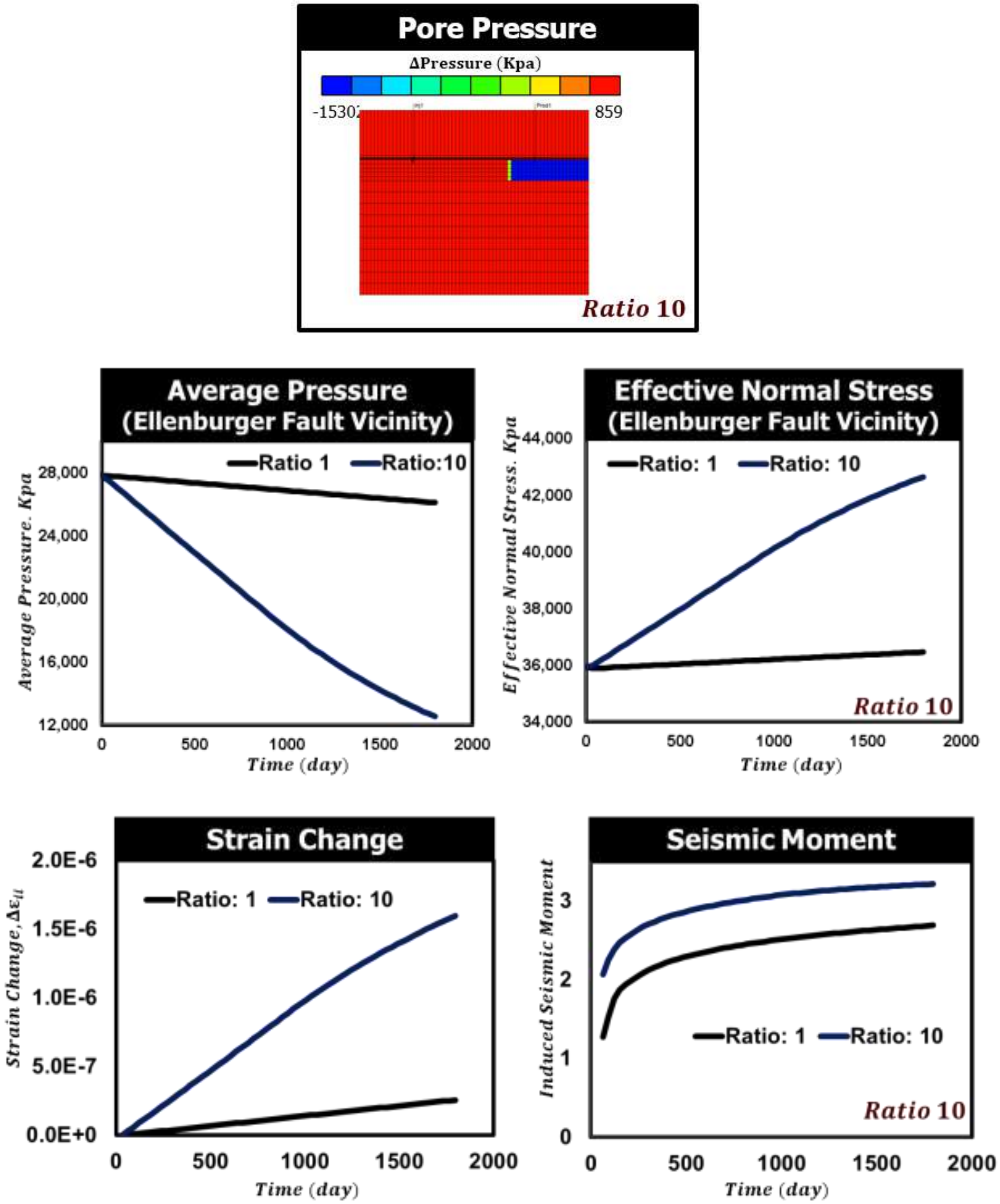

Fig. 25 – Basement Strain Change, Induced Seismicity, Stress, and Pressure for Ratio: 10

Similar unbalanced cases were reproduced in Abaqus to study the production-injection ratio change effects on strain change and seismicity for comparison. The same setup from CMG was replicated in Abaqus, as closely as possible within the limits of software capability and flexibility, to compare the basement strain change, induced seismicity, and average pressure within the vicinity of the fault. Fig. 26 through Fig. 28 below compare the basement strain change, induced seismicity and the corresponding pore pressure changes between Abaqus and CMG at the end of simulation as the ratio of production rate to injection rate was increased. As the rate of production to injection ratio was increased, more compaction occurred in the target “C” formation, and the strain change increased monotonically with a larger pore pressure difference at the end of the five year period. For the base case in Fig. 26, there is a decline in the average pore pressure because the fault which is closer to the producer has a much smaller permeability compared to the permeability of the entire target formation and there is consequently less pore volume on the right producer region compared to the left injector region within the target formation. Abaqus and CMG pore pressure, basement strain change and induced seismicity results are fairly similar in the base case.

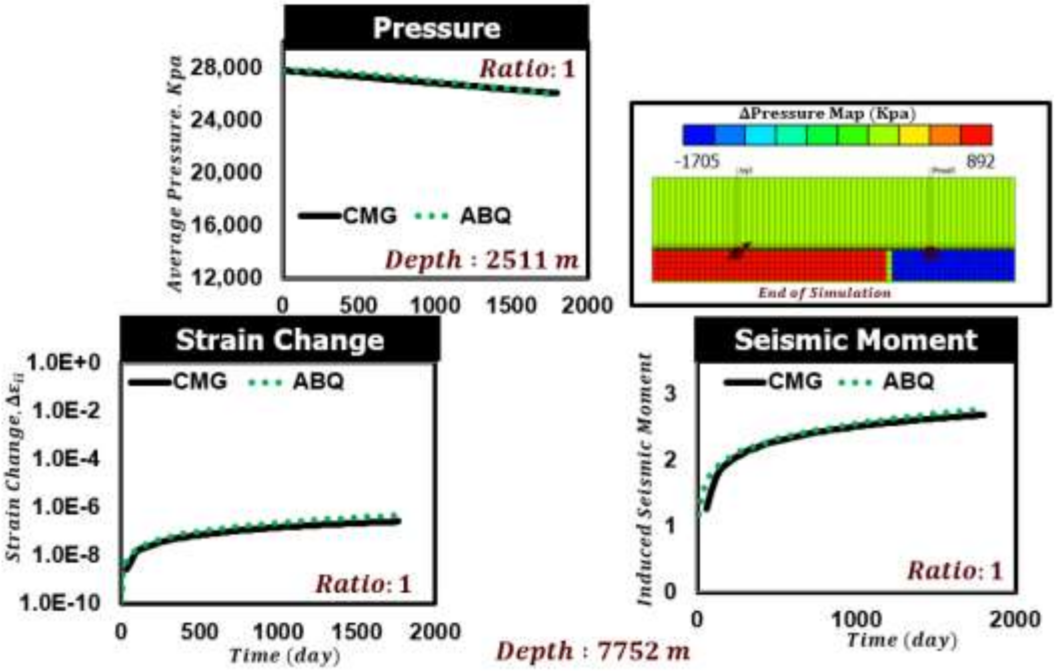

Fig. 26 – ABQ vs CMG: Basement Strain Change, Induced Seismicity, Pressure at Ratio: 1

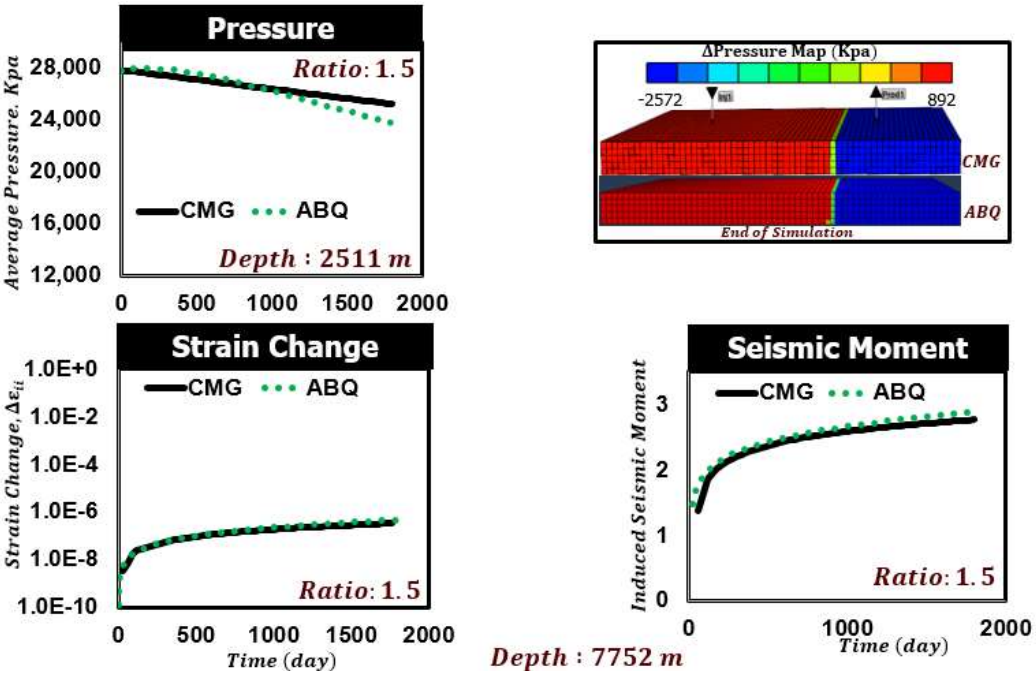

Fig. 27 –ABQ vs CMG:Basement Strain Change, Induced Seismicity, Pressure at Ratio: 1.5

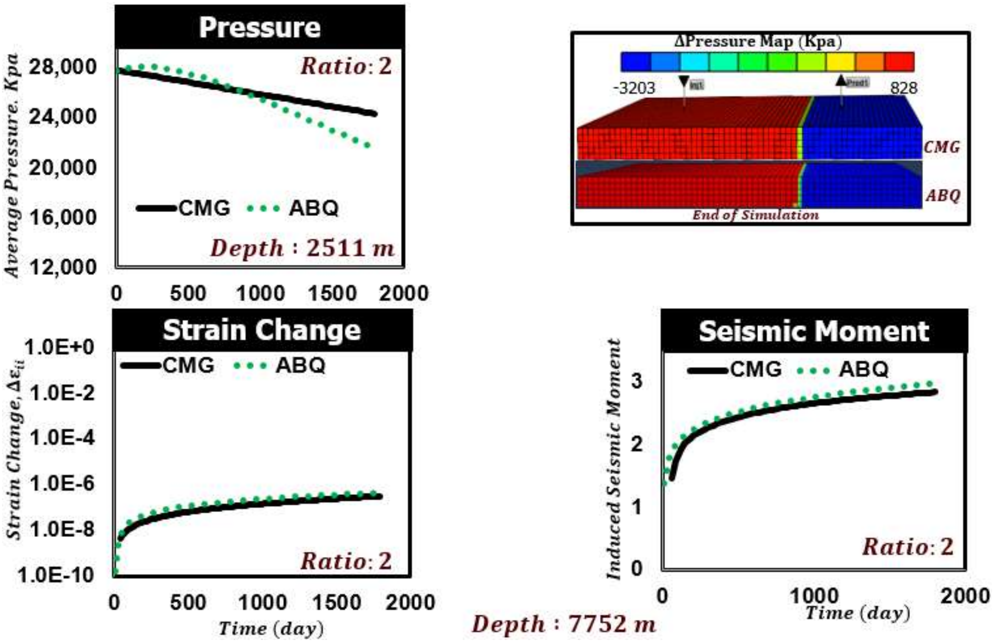

Fig. 28 – ABQ vs CMG: Basement Strain Change, Induced Seismicity, Pressure at Ratio: 2

For the unbalanced cases in Fig. 27 and Fig. 28, a similar trend is observed for the basement strain change and induced seismicity in both Abaqus and CMG. The average pore pressure response near the fault as indicated by the accompanied pressure maps in Abaqus drops faster than in CMG due to the location of the well. The production and injection wells are placed at the cell center in CMG versus placed at a corner node on the corresponding production or injection cell. Even though both models show the same trend in pore pressure, basement strain change, and induced seismicity, as the ratio of production to injection rate increases, the Abaqus and CMG results (especially pore pressure) become less similar. This difference is partly due to fault representation discrepancy between both simulators and because the difference between cell volume-based output (CMG) and nodal-based output (Abaqus) become more pronounced with increasing ratio. The rise in pore pressure above the undrained initial value at early times, before the onset of decline, for the unbalanced cases in Fig. 27 and Fig. 28 could occur as a result of stress transfer to the cell interior, otherwise known as the Mandel-Cryer phenomenon. This phenomenon has been explained by Wang (2000) using a canonical demonstration of how finite element poroelastic coupling can produce non-monotonic pore pressure behavior following undrained conditions in hydrostatic loading at the center of a long rectangular plate sandwiched within two rigid bodies. For the example of the hydrostatic loading of a plate, contraction of the drained edges (due to pore pressure dissipation) induce an additional pore pressure build up in the interior of the plate according to the principle of strain compatibility. This causes the pore pressure increase above an undrained value for small dimensionless times (early times) before pore pressure decline eventually occurs. However, in this current study, the portion of the fault in target zone “C” was removed to test if fault representation disparity between Abaqus and CMG had any impact on the basement strain change, induced seismicity and pore pressure sensitivity study. As seen in Fig. 29 through Fig. 31, when the fault is removed from the target zone “C” for the same sensitivity study of the basement strain, induced seismicity and pore pressure conducted from Fig. 26 through Fig. 28, a better match is observed in pore pressure change, strain change and induced seismicity between Abaqus and CMG results. This suggests that the difference in fault representation between Abaqus (nodal-based) and CMG (cell-based) is a possible source for the discrepancy in pore pressure (average near the vicinity of the fault), strain change and induced seismic sensitivity results between both simulators. Note that if the average pressure for the entire target formation “C” is compared between Abaqus and CMG when the fault is removed, a similar pressure decline trend is expected from both simulators as the ratio of production to injection rate increases. Hence, the difference in the local average pressure near the vicinity of the fault between Abaqus and CMG, when the fault is present in the target formation is due to local transients as suggested by Mandel-Cryer effect. This idea requires more investigation to arrive at a conclusive assertion.

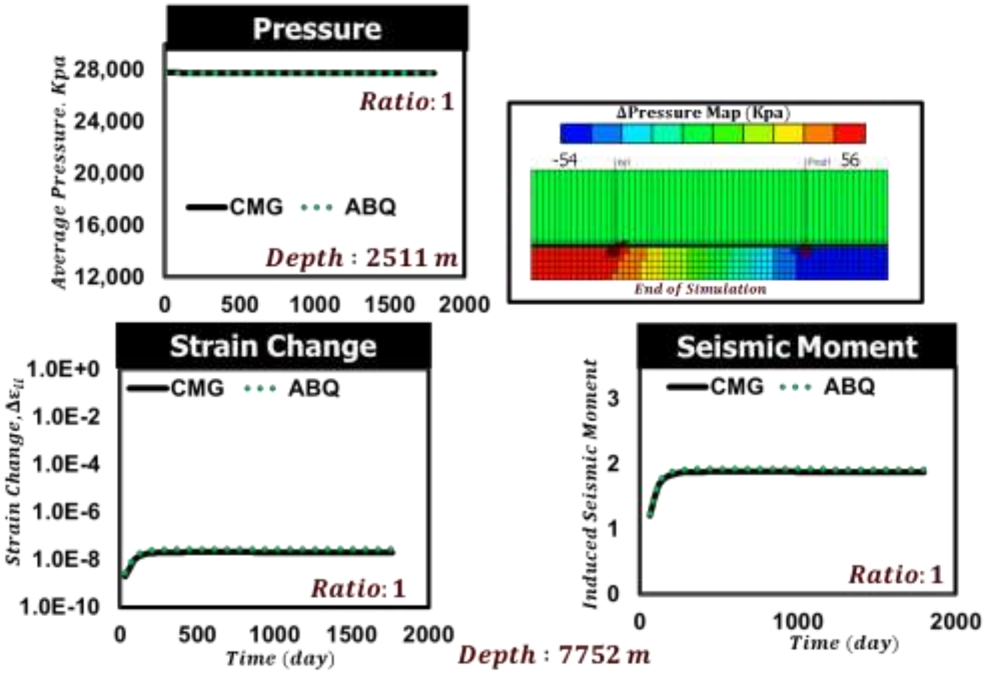

Fig. 29 – ABQ vs CMG (No Fault): Strain Change, Seismicity, Pressure at Ratio: 1

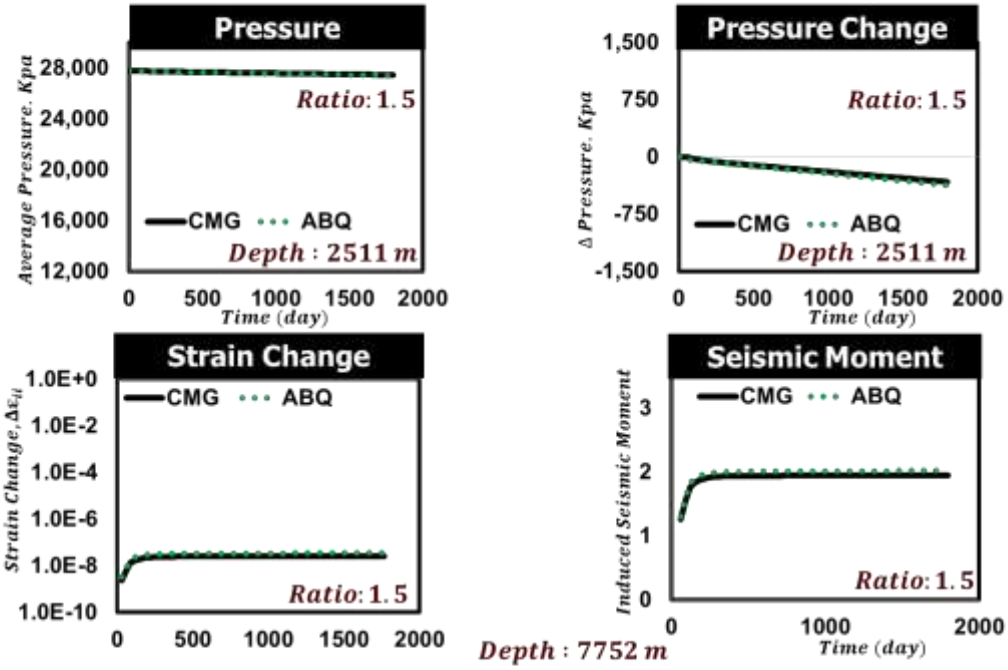

Fig. 30 – ABQ vs CMG (No Fault): Strain Change, Seismicity, Pressure at Ratio: 1.5

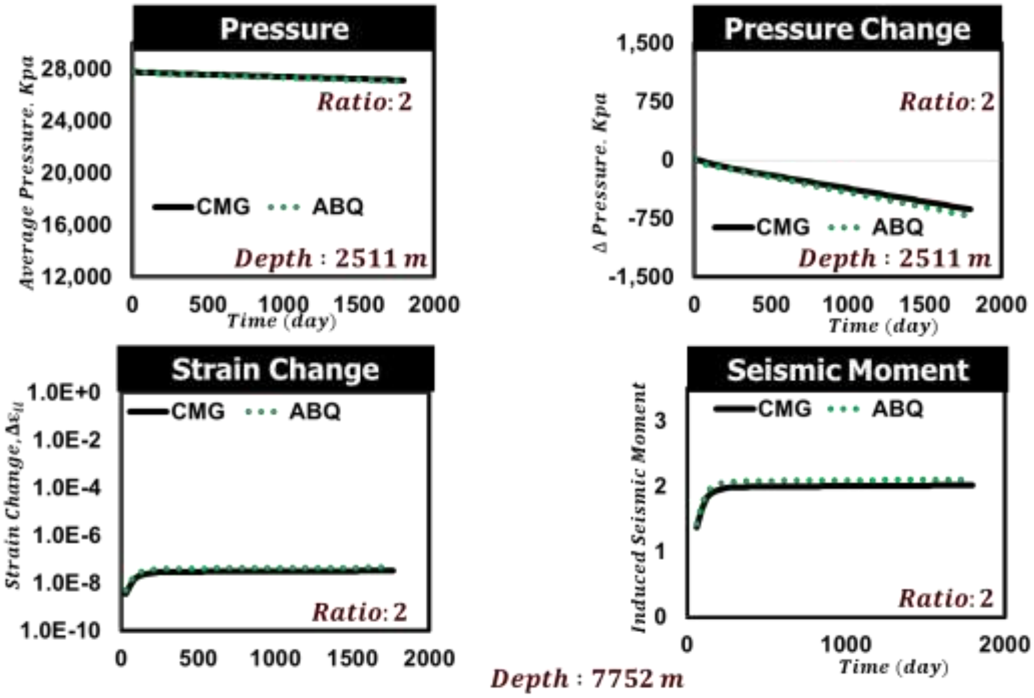

Fig. 31 – ABQ vs CMG (No Fault): Strain Change, Seismicity, Pressure at Ratio: 2

4.3 Fault Permeability Effects on Basement Strain Change

The effect of fault permeability on the pore pressure distribution and strain change will be examined to observe stability in the presence and absence of a fault. The effect of reservoir injection layer permeability on pore pressure distribution near the vicinity of the wells will be examined over time for different reservoir target formation properties admissible in the test models. Consider the base case, where the same injection and production rates of $416.67\frac{m^3}{day}$ flow through the "C" formation, while all properties remain constant. The fault permeability was varied from a strong barrier of $3 \times 10^{-3}\ md$ to a porous weak fault of $30\ md$. Fig. 32 through Fig. 36 show the basement strain change at depth $7752\ m$ and corresponding pore pressure change at the end of a five year period in the "C" target formation as a result of increasing fault permeability. As the fault permeability is increased by one order of magnitude per scenario below, increasing communication occurs between the injection and production sections of the "C" target formation and steady state conditions are approached. The pressure difference gets smaller as the fault permeability increases and the strain change diminishes over time and stabilizes to a flat horizontal line when enough leakage occurs and steady state is reached. This happens when the fault permeability has reached the permeability of the target "C" formation.

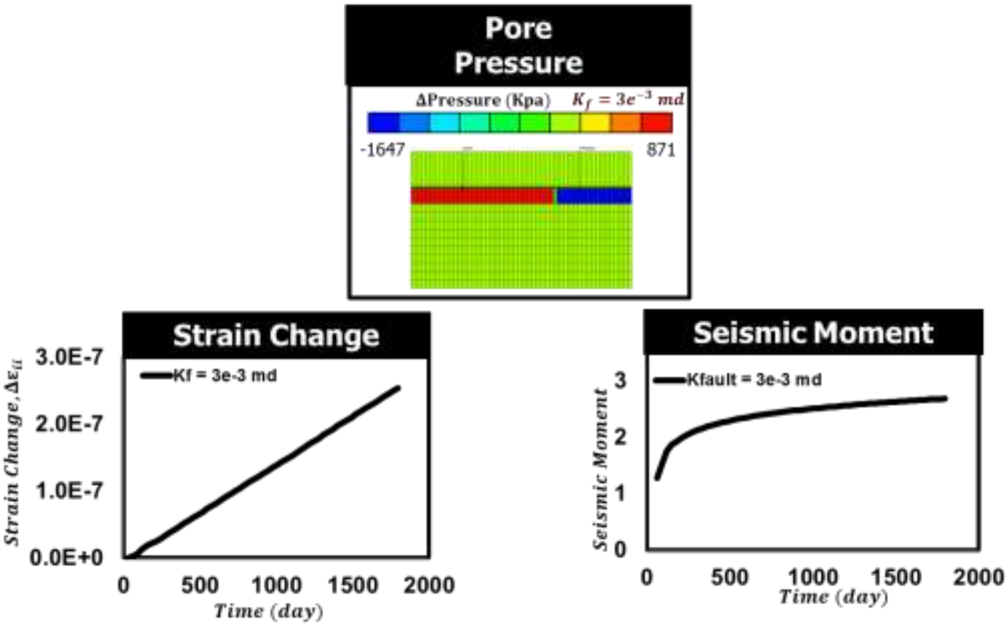

Fig. 32 – Strain Change and Pore Pressure Change for fault permeability: $k_f = 0.003\ md$

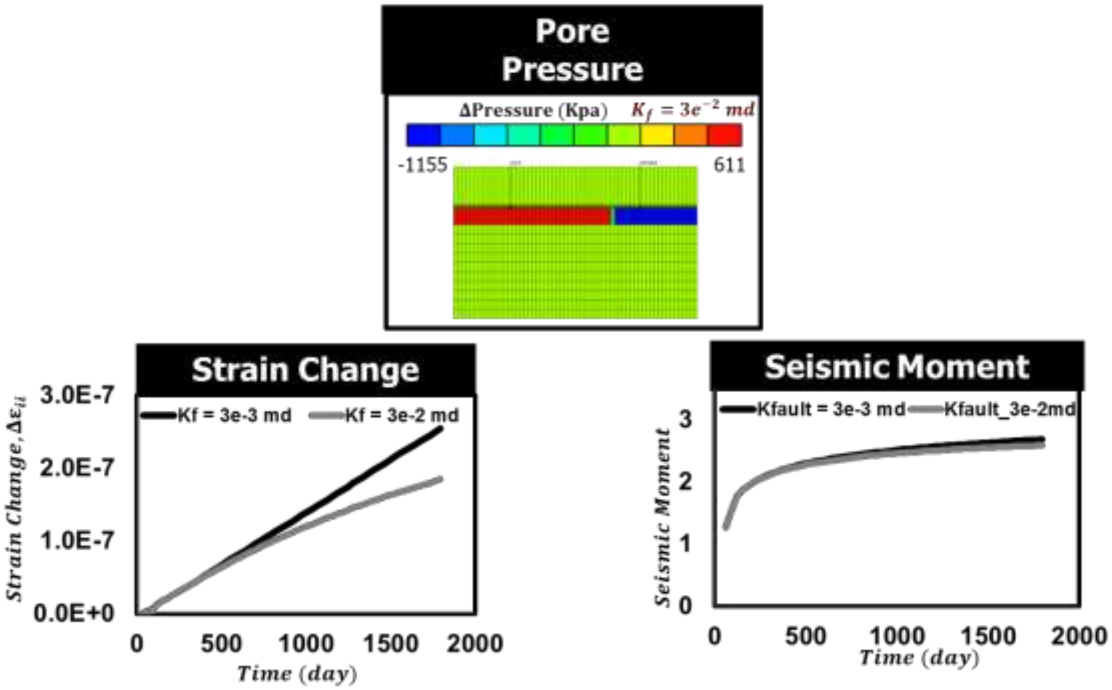

Fig. 33 – Strain Change and Pore Pressure Change for fault permeability: $k_f = 0.03\ md$

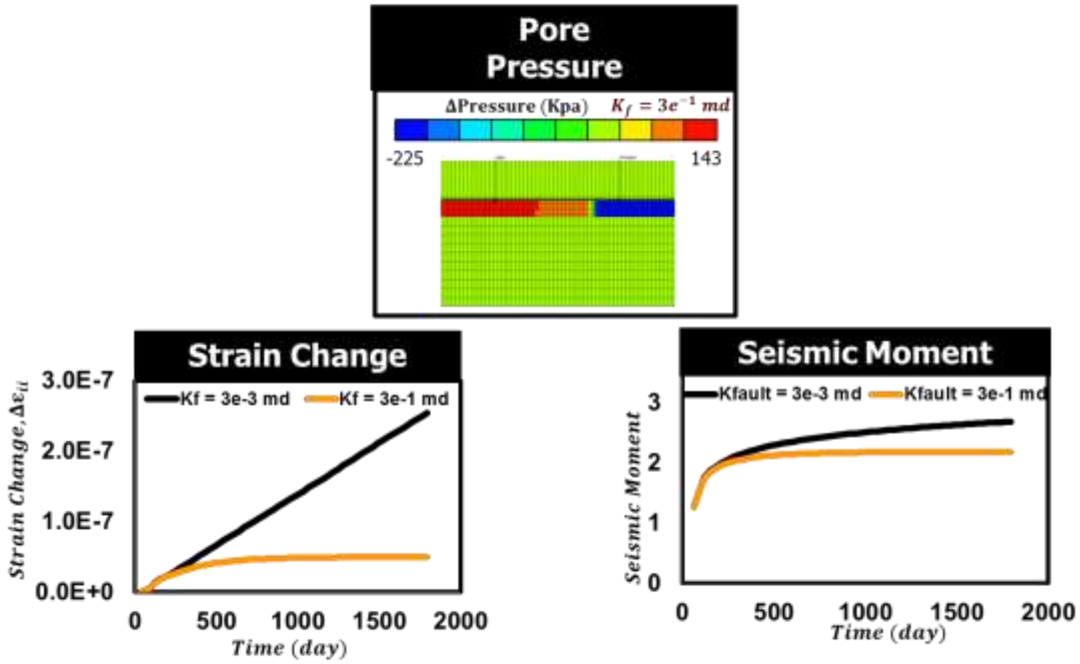

Fig. 34 – Strain Change and Pore Pressure Change for fault permeability: $k_f = 0.3\ md$

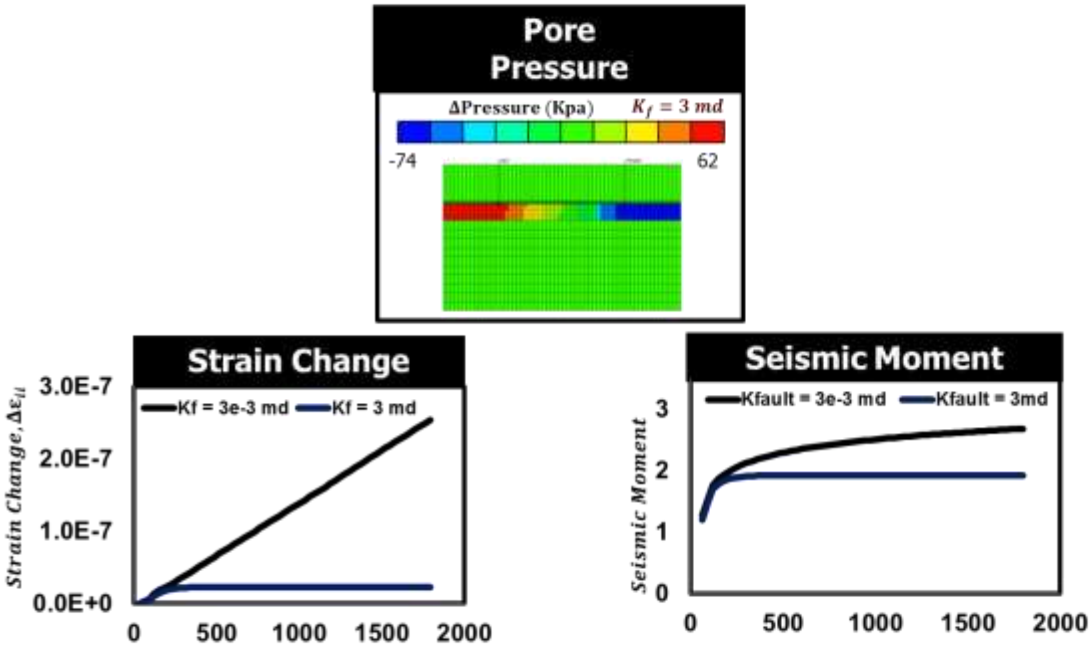

Fig. 35 – Strain Change and Pore Pressure Change for fault permeability: $k_f = 3\ md$

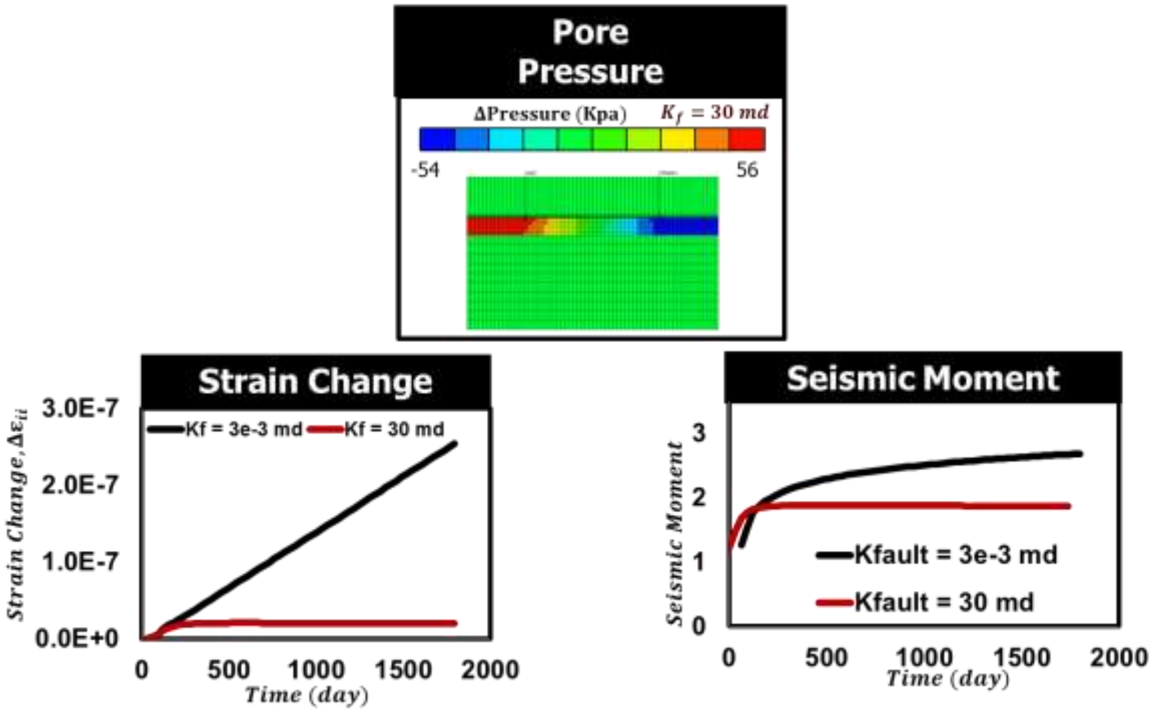

Fig. 36 – Strain Change and Pore Pressure Change for fault permeability: $k_f = 30\ md$

CHAPTER V

CONCLUSIONS AND RECOMMENDATIONS

5.1 Conclusions

Coupled fluid flow with geomechanics is necessary for complex stability phenomena. Results suggest that a combination of fluid flow and geomechanical effects can have an impact on basement strain change and induced seismicity. The specific conclusions from this research can be summarized as follows. Coupled fluid flow and geomechanical formulations have been reviewed. Results from two commercial simulators using the finite difference versus finite element approach were compared to show that both fluid flow and geomechanical properties can have an impact on basement strain change and induced seismicity. Results suggest that the discrepancy in pore pressure, strain change and induced seismic moment sensitivity studies between Abaqus and CMG results in this work are due to fault representation differences. Varying the production-injection activity scenario has implications on basement strain change, target zone average pressure (near fault vicinity), and induced seismic activity. Near fault basement strain change depends more on production pattern variation compared to injection pattern variation as more compaction occurs. Unbalanced target formation Injection-production activity can lead to increased strain change and seismicity in the basement. Results show that the strain change and induced seismicity in the reservoir basement increase as the ratio of target formation production to injection rate increases. Induced seismicity is more related to strain change as opposed to only pore pressure change.

5.2 Recommendations

Coupled fluid flow with geomechanics simulation is necessary for proper modeling of hydro-mechanical processes in the oil and gas industry such as waste water injection. The Abaqus and CMG test models used in this study are a simplification of the Azle case study assuming a one injection and one production well with a single element block in the y direction. The next step in the possible expansion of this research work is to look at compaction failure as a result of an increase in maximum principal stress. An extension of the working Abaqus and CMG test models to a full scale Azle field case with two injectors and seventy producers in order to account for the more complex geomechanics effects in an unbalanced injection-production study can be attempted. However, there is a challenge with realizing a full scale Azle model in Abaqus due to the difficulty and tedious nature in precise definition of multiple wells and the absence of the ability to specify well completion and operation schedule when compared to CMG. Another way to approach the development of coupled model for induced seismicity study is to develop a simulation code from scratch based on the fundamental equations, discretization and coupling techniques for flexibility. However, this approach is much more time consuming and requires a deeper undersanding of the finite element and finite difference discretization methods. The goal for the full scale Azle study is to further illustrate the necessity for coupled poroelastic model to explain complex geomechanics interaction in the reservoir basement and induced seismicity due to an unbalanced production-injection operations in areas with underlying fault systems. The overall significance and value of this research project to the industry is to provide a basic idea of reservoir geomechanics implications as well as guidance on best practices regarding waste water injection especially in areas with previous seismic history.

REFERENCES

Abaqus (2014), Abaqus User's Guide and Help Documentation, Version 6.14, SIMULIA Company, Providence.

Aki, K., & Richards, P. G. (2002). *Quantitative seismology*, second edition (Vol.1).

Chen, R., et al. (2018). Coupled Fluid Flow and Geomechanical Modeling of Seismicity in the Azle Area (North Texas). In *SPE Annual Technical Conference and Exhibition*. Society of Petroleum Engineers.

Dean, R. H., Gai, X., Stone, C. M., & Minkoff, S. E. (2006). A comparison of techniques for coupling porous flow and geomechanics. *Spe Journal*, *11*(01), 132-140.

Denney, D. (2006). Iterative coupling between geomechanical deformation and reservoir flow. *Journal of petroleum technology*, *58*(09), 102-105.

Fan, Z., Eichhubl, P., & Gale, J. F. (2016). Geomechanical analysis of fluid injection and seismic fault slip for the Mw4. 8 Timpson, Texas, earthquake sequence. *Journal of Geophysical Research: Solid Earth*, *121*(4), 2798-2812.

Fjaer, E., Horsrud, P., Raaen, A. M., Risnes, R., & Holt, R. M. (1992). *Petroleum related rock mechanics* (Vol. 33). Elsevier.

Frohlich, C., Hayward, C., Stump, B., & Potter, E. (2011). The Dallas–Fort Worth earthquake sequence: October 2008 through May 2009. *Bulletin of the Seismological Society of America*, *101*(1), 327-340.

González, P. J., Tiampo, K. F., Palano, M., Cannavó, F., & Fernández, J. (2012). The 2011 Lorca earthquake slip distribution controlled by groundwater crustal unloading. *Nature Geoscience*, *5*(11), 821-825.

Hornbach, M. J., DeShon, H. R., Ellsworth, W. L., Frohlich, C., ... & Luetgert, J. H. (2015). Causal factors for seismicity near Azle, Texas. *Nature communications*, *6*.

Jha, B., & Juanes, R. (2007). A locally conservative finite element framework for the simulation of coupled flow and reservoir geomechanics. *Acta Geotechnica*, *2*(3), 139-153.

Kanamori, H. (1977). The energy release in great earthquakes. *Journal of geophysical research*, *82*(20), 2981-2987.

Keller, G. R., & Holland, A. (2013). Oklahoma Geological Survey evaluation of the Prague earthquake sequence of 2011. *Oklahoma Geological Survey, Norman, OK*.

Li, P., & Chalaturnyk, R. J. (2006). Permeability variations associated with shearing and isotropic unloading during the SAGD process. *Journal of Canadian Petroleum Technology*, *45*(01).

Lund Snee, J. E., & Zoback, M. D. (2016). State of stress in Texas: Implications for induced seismicity. *Geophysical Research Letters*, *43*(19).

Minkoff, S. E., Stone, C. M., Bryant, S., Peszynska, M., & Wheeler, M. F. (2003). Coupled fluid flow and geomechanical deformation modeling. *Journal of Petroleum Science and Engineering*, *38*(1-2), 37-56.

Morita, N. (2015). Finite element method for geomechanics problems in oil industries. *Texas A&M University*.

Redmayne, D. W. (1988). Mining induced seismicity in UK coalfields identified on the BGS National Seismograph Network. *Geological Society, London, Engineering Geology Special Publications*, *5*(1), 405-413.

Rubinstein, J. (2015). Yes, Humans Really Are Causing Earthquakes. *U.S. Geological Survey*.

Event occurs at 15:22, 20:25 and 36:28. https://online.wr.usgs.gov/calendar/2015/aug15.html. Accessed June 13, 2018.

Rutqvist, J., Rinaldi, A. P., Cappa, F., & Moridis, G. J. (2013). Modeling of fault reactivation and induced seismicity during hydraulic fracturing of shale-gas reservoirs. *Journal of Petroleum Science and Engineering*, *107*, 31-44.

Settari, A., & Mourits, F. M. (1998). A coupled reservoir and geomechanical simulation system. *Spe Journal*, *3*(03), 219-226.

Simpson, D. W., Leith, W. S., & Scholz, C. H. (1988). Two types of reservoir-induced seismicity. *Bulletin of the Seismological Society of America*, *78*(6), 2025-2040.

Tran, D., Nghiem, L., & Buchanan, L. (2005, January). Improved iterative coupling of geomechanics with reservoir simulation. In *SPE Reservoir Simulation Symposium*. Society of Petroleum Engineers.

Tran, D., Settari, A., & Nghiem, L. (2004). New iterative coupling between a reservoir simulator and a geomechanics module. *Spe Journal*, *9*(03), 362-369.

Wang, H. F. (2000). Theory of linear poroelasticity with applications to geomechanics and hydrogeology, Princeton University Press.

APPENDIX A

CMG FORMULATION DETAILS

A.1 Fluid Flow

CMG employs the finite difference approach for sequentially solving the fluid flow equations and then the geomechanics equations via discretized newton iterations. Darcy's law relates the apparent superficial fluid velocity ($\upsilon = \frac{q}{A}$) to the fluid potential(Φ).

$$\frac{q}{A} = -\frac{k}{\mu_f}\nabla\Phi \tag{A.1}$$

Where the fluid potential is given by

$$\Phi = p - \gamma z \tag{A.2}$$

For the 2D case considered in this study, only the contribution of fluid pressure is considered for the flow potential. Darcy's law simplifies to becomes

$$\upsilon = -\frac{k}{\mu_f}\nabla p \tag{A.3}$$

The above version of Darcy's law assumes a non-Darcy coefficient of 1 for fluids deviating from ideal conditions.

The governing conservation equation for a single-phase flow in general is given as follows:

$$\frac{\partial\left(\phi\rho\right)}{\partial t} = \nabla\left(\rho\upsilon\right) + q \tag{A.4}$$

The above assumes a homogenous and isotropic reservoir system, neglecting the effect of gravity with constant reservoir and fluid properties. For a slightly compressible fluid, the reservoir fluid density (ρ) and formation volume factor $\left(B_f\right)$ can be described as functions of fluid pressure at a current and initial states as well as fluid compressibility.

$$\rho = \rho_i \left[1 + c_f \left(p - p_i\right)\right] \tag{A.5}$$

$$B_f = \frac{B_{f_i}}{\left[1 + c_f \left(p - p_i\right)\right]} \tag{A.6}$$

For slightly compressible rock, then the porosity varies with pressure. Hence the rock compressibility (c_R) is given by:

$$c_R = \frac{\left(\frac{\phi}{\phi_i} - 1\right)}{p - p_i} \tag{A.7}$$

The conservation principle needs to be modified in order to account for deformations. Assuming that the simulator grid is attached to and deforms with the porous medium such that the bulk volume and volumetric strain apply equally to all grid cells in the simulated system. The altered conservation of fluid in a deformable porous medium (Denney et al 2006) is given by:

$$\frac{\partial}{\partial t}\left[\phi \rho_f \left(1 - \epsilon_v\right)\right] - \nabla \cdot \left(\rho_f \frac{k}{\mu_f} \cdot \left[\nabla p - \rho_f b\right]\right) = Q_f \tag{A.8}$$

Where ρ_f is the fluid density, ϵ_v is the volumetric strain, b is the body force per unit mass of fluid, k is the permeability, μ_f is the fluid viscosity, Q_f is the flow rate of fluid at source or sink location, and $\phi = \frac{V_p}{V_b}$ is the true porosity (Settari et al 1998) defined as the ratio of the current pore volume to the current bulk volume. The volumetric strain defined in the altered mass conservation flow equation allows the conservation principle to account for the changes in the porous media bulk volume. In order to incorporate the porous media deformation into a conventional simulator, Denney et. al (2006) propose a “reservoir porosity” term (ϕ^*) which is a function of the volumetric strain to replace the true porosity in the altered mass conservation principle equation.

$$\phi^* = \left(1 - \varepsilon_v\right)\phi \tag{A.9}$$

Therefore the altered mass conservation equations which can be implemented as the final fluid flow equation in a conventional simulator becomes:

$$\frac{\partial}{\partial t}\left[\phi^* \rho_f\right] - \nabla \, . \left(\rho_f \, \frac{k}{\mu} . \left[\nabla p - \rho_f b\right]\right) = Q_f \tag{A.10}$$

The above expression now accounts for the porous media deformation by virtue of the reservoir porosity term which acts as the link (coupling parameter) between the fluid flow and geomechanics equations in CMG.

In a similar fashion, the energy conservation principle for a reservoir system with time variant temperatures can be described as a function of the reservoir porosity term.

$$\frac{\partial}{\partial t}\left[\phi^* \rho_f U_f + \left(1 - \phi^*\right)\rho_r U_r\right] + \nabla \, . \left[-\rho_f \, \frac{k}{\mu} . \left[\nabla p - \rho_f b\right] H_f\right] + \nabla \, . \left[\kappa \nabla \mathrm{T}\right] = Q_h \tag{A.11}$$

Where Q_h is the heat loss/gain, T is the temperature, κ is the thermal conductivity, ρ is density while U_f and U_r are the fluid and rock enthalpies respectively. However, in this study the energy conservation principle is not employed because it is assumed that temperature changes over time are insignificant which may not necessarily be the case in reality.

A.2 Geomechanics

Assuming a homogenous, isotropic and symmetric material with a very small strain compared to unity, the geomechanical force equilibrium equation states that the gradient of the total stress tensor is balanced by the sum of all the body force which accounts for gravity.

$$\nabla . \vec{\sigma} - B = 0 \tag{A.12}$$

The kinematic strain-displacement relationship, which is approximated from the Green-Lagrange infinitesimal strain tensor, is given by

$$\overleftrightarrow{o} = \frac{1}{2}\left[\nabla \vec{u} + \left(\nabla \vec{u} \right)^{T} \right] \tag{A.13}$$

From the concept of effective stress, the constitutive stress-strain relationship applies

$$\vec{\sigma} = \vec{C} : \overleftrightarrow{o} + \alpha \text{ p I} \tag{A.14}$$

Where the tangential stiffness tensor is given by

$$\vec{C} = \frac{E(1-v)}{(1+v)(1-2v)} \begin{bmatrix} 1 & \frac{v}{(1-v)} & \frac{v}{(1-v)} & 0 & 0 & 0 \\ \frac{v}{(1-v)} & 1 & \frac{v}{(1-v)} & 0 & 0 & 0 \\ \frac{v}{(1-v)} & \frac{v}{(1-v)} & 1 & 0 & 0 & 0 \\ 0 & 0 & 0 & \frac{(1-2v)}{2(1-v)} & 0 & 0 \\ 0 & 0 & 0 & 0 & \frac{(1-2v)}{2(1-v)} & 0 \\ 0 & 0 & 0 & 0 & 0 & \frac{(1-2v)}{2(1-v)} \end{bmatrix} \tag{A.15}$$

Substituting the kinematic strain-displacement relationship and the constitutive stress-strain relationship into the geomechanics force equilibrium equations, the final geomechanics combined formulation becomes

$$\nabla\left[\vec{C}:\left(\frac{1}{2}\left(\nabla u+\left(\nabla u\right)^{T}\right)\right)\right]=-\nabla\alpha\ \mathrm{p}\ \mathrm{I}+\rho \mathrm{g} \tag{A.16}$$

According to the CMG STARS solution guideline manual, given an applied force, the displacement equation is first solved to obtain displacements. Results go into the kinematic strain-displacement relationship to obtain the stress tensor after which the constitutive stress-strain relationship is employed to obtain the effective stress tensor.

A.3 Two-Way Iterative Coupling Using Finite Difference Approach

The two-way finite difference iteratively coupled strategy between CMG STARS and the geomechanics module is explored in SPE 97879 (Tran et. al 2004, 2005). However only parts pertinent to the coupled fluid flow-geomechanics formulation are provided within the context and scope of the current study. As discussed in Appendix A.1, the “reservoir porosity” coupling term (ϕ^{*}) which is a function of the volumetric strain, makes the two-way (sequential or iterative) coupling process possible. The linearized equivalent form for the discretization of the reservoir porosity two-way coupling term can be expressed as a function of formation compressibility coefficient (c_n^o) while accounting for the entire grid’s geomechanical response to pressure change calculated in the geomechanics module.

$$\phi^*_{(n+1)} = \phi^*_{(n)} + c_n^0 \left(p_{(n+1)} - p_{(n)} \right) \qquad \text{(A.17)}$$

Where (n) and $(n+1)$ are the time step counter for the current and next time steps.

$$c_n^0 = \left(\left[c_0 \right] + \left[c_2 \times a_1 \right] \right)_n \qquad \text{(A.18)}$$

$$\therefore c_n^0 = \left(\left[\frac{1}{V_B^0} \left(\frac{dV_p}{dp} + V_B \alpha c_b \frac{d\sigma_m}{dp} \right) \right] + \left[\left(-\frac{V_p}{V_B^0} \alpha c_b \right) \times \left(\Gamma \left\{ \frac{2}{9} \frac{E}{(1-\nu)} \left(c_b - c_r \right) \right\} \right) \right] \right)_n \qquad \text{(A.19)}$$

Where α is the biot number, σ_m is the mean stress, c_b is the bulk compressibility, c_r is the solid rock compressibility, Γ is the boundary constrained factor while V_B and V_P are the current bulk volume and pore volumes respectively. It is important to note the temperature effects in the above compressiblity coefficient and discretized reservoir porosity formulation has been neglected within the scope of the current study and only pressure terms are included in the above discretization.

The following formulation describes the process of updating permeability due to shearing. Changes in permeability with stress and strain can be measured by laboratory experiments and determined as a function of porosity or volumetric strain or mean stress. The absolute permeability due to shearing can be defined empirically as a function of volumetric strain from (Li et al., 2006) as follows:

$$\ln\left(k / k_0 \right) = C_{n1} \epsilon_v \qquad \text{(A.20)}$$

Where k and k_0 are, respectively, the permeability at the current sheared and initial conditions and ϵ_v is the volumetric strain. Li et al., 2006 derives the Touhidi-Baghini parameter (C_{n1}) to yield:

$$C_{n1} = \left[\frac{(1-\phi_0)\, a + b\phi_0}{\phi_0} \right] \tag{A.21}$$

a and b are constants which are determined from experimental data. Assuming both constants are equal according to the Chardabella terms $(a = b = C_{ab})$, the empirical permeability relationship due to shearing can be written as:

$$\ln(k / k_0) = \frac{C_{ab}}{\phi_0} \grave{o}_v \tag{A.22}$$

After discretization, the fluid flow equations can be partitioned as shown below

$$\begin{bmatrix} B_2 & 0 \end{bmatrix} \left[\vec{p} \right] = \left[D_2 \right] --- FluidFlow \tag{A.23}$$

While the geomechanics equations are partitioned as

$$\left[A_1 \right] \left[\vec{u} \right] = \left[E_1 \right] --- Geomechanics \tag{A.24}$$

Where A_1 is the stiffness matrix and E_1 is the load vector for the geomechanics part while B_2 and D_2 are the transmissibility-accumulation and source-sink terms respectively for the fluid flow part. The final fluid flow and combined geomechanics equations are numerical solved by imposing time stepping on a grid to obtain the discrete pressure and displacement unknowns. In the iterative sequential (two-way) coupled approach, for a given tur porosity and volumetric strain values, the pressure for each grid cell is solved first from the final fluid flow equation before the displacement is solved from the geomechanics combined formulation. The conservation principle is inherently satisfied in the above two-way coupling approach because when the altered fluid flow equation converges, the current updated coupling parameter of the newton iteration (ϕ_k^*) is equal to (ϕ_{n+1}^*)

and hence the reservoir porosity is conserved (an update in geomechanics coefficients does not change the reservoir porosity or violate conservation principle).

The two-way iteratively coupled approach used is CMG is different from the fully coupled approach because the pressure and displacement unknown variables are solved separately with feedback, not simultaneously. The pressure solution from the fluid flow discretized module is fed into the discretized geomechanical module where the displacement solution is obtained. The iterative two-way coupling is made possible via the coupling parameter instead of a coupling from simultaneous discretized matrix equations as occurs in the fully coupled scenario.

APPENDIX B

ABAQUS FORMULATION DETAILS

B.1 Fluid Flow

While the same fundamental fluid flow and geomechanics equations are solved in both Abaqus and CMG, the method of discretization and coupling are different. Abaqus employs the finite element method using gauss integration point formulation, interpolated shape functions, and backward Euler approximation to simultaneously solve a system of equations both pressure and displacement. However only parts pertinent to the coupled fluid flow-geomechanics formulation are provided within the context and scope of the current study. Another more general representation of the porous media fluid flow description (analogous to Darcy's law) known as Forchheimer's law is employed as illustrated in the Abaqus theory guide. According to Forchheimer's law, high flow velocities can reduce the effective permeability and lead to a choked pore fluid flow. For pore fluid flow, Forchheimer's law can be written as follows:

$$\vec{\dot{Q}}\left(1+\beta\sqrt{\overrightarrow{V_w}.\overrightarrow{V_w}}\right)=-\frac{k_s}{\gamma_w}k.\left(\frac{\partial P_w}{\partial\vec{x}}-\gamma_w\right) \tag{B.1}$$

Where $\overrightarrow{\dot{Q}}$ is the volumetric flow rate per unit area of a particular wetting fluid, $\overrightarrow{V_w}$ is the fluid velocity, β is a velocity coefficient, k and k_s are the permeability of a fully saturated medium and dependence of permeability on the saturation of the wetting fluid $(k_s|_{s=1} = 1)$, while P_w and γ_w are the wetting fluid pore pressure in spatial coordinate $\vec{x}$ and specific weight respectively. At low fluid flow velocities $(\beta = 0)$, Forchheimer's law becomes a good approximation of the well-known aforementioned Darcy flow.

$$\dot{\vec{Q}} = -\frac{Ҡ}{\gamma_w}\left(\frac{\partial P_w}{\partial \vec{x}} - \gamma_w\right) \tag{B.2}$$

Where Ҡ is the hydraulic conductivity, γ_w and ρ_w are the specific weight and density of the wetting fluid, μ_f is the fluid viscosity, g is the gravitational constant while k is the permeability of the rock. For soils consolidation problems like the one in this study, the fully saturated permeability is given as a function of void ratio. Comparing the above Forchheimer expression at low pore fluid flow velocities in relation to the Darcy Law, a simplified expression for the hydraulic conductivity-permeability relationship can be obtained. The hydraulic conductivity $(Ҡ)$, the term through which permeability is defined in Abaqus, is then defined as a function of permeability(k).

$$Ҡ = \frac{\gamma_w\, k}{\mu_f} = \frac{\rho_w g\, k}{\mu_f} \tag{B.3}$$

The final Forchheimer law form equivalent to Darcy's law is given by

$$\dot{\vec{Q}} = -Ҡ(\nabla H) \tag{B.4}$$

Where H is the dimensionless head.

The continuity equation, required to equate the rate of increase of in the fluid mass stored at a node to the rate of mass of fluid flowing into the node within a given time increment, is integrated in time using the backward Euler approximation. This equation is satisfied approximately in the finite element model by using excess wetting liquid pressure (P_w) as the nodal variable interpolated over the elements. The total derivative of the integrated variational form of the continuity statement with respect to the nodal variables is required for the newton iterations employed for solving non-linear, coupled, equilibrium equations.

For a relatively incompressible wetting liquid in a porous medium, the continuity equation in terms of the finite element approximation variational form equates the time rate of change of a given mass of wetting fluid to the addition of fluid mass across the surface.

$$\int_V \frac{1}{J}\frac{d}{dt}\left(J\,\rho_w\left(n_w+n_t\right)\right)dV = -\int_S\left(\rho_w n_w \vec{n}\cdot\overrightarrow{V_w}\right)dS \qquad \text{(B.5)}$$

The nodal continuity statement by virtue of the divergence theorem for an arbitrary volume, can be written as:

$$\frac{1}{J}\frac{d}{dt}\left(J\,\rho_w\left(n_w+n_t\right)\right)+\frac{\partial}{\partial\vec{x}}\left(\rho_w n_w\overrightarrow{V_w}\right)=0 \qquad \text{(B.6)}$$

Where $\overrightarrow{V_w}$ is the average velocity of the wetting fluid relative to the solid phase (seepage velocity), J is the ratio of the fluid volume in the current configuration to the fluid volume in the reference configuration, $\vec{n}$ is the outward normal to the surface (S), ρ_w is the density of the wetting fluid, n_w and n_t are the volume ratio of free wetting fluid and the volume ratio of trapped fluid at a point. Rewriting the above expression in the weak form, and employing an arbitrary continuous wetting fluid pore pressure variational field test function (δP_w), Abaqus solves the continuity statement normalized with the wetting fluid density at a reference state $\left(\rho_w^i\right)$ by integrating approximately in time using the backward Euler formula:

$$\begin{aligned}\int_V\left[\delta P_w\left(\frac{\rho_w}{\rho_w^i}\left(n_w+n_t\right)\right)-\frac{1}{J}\left(\frac{\rho_w}{\rho_w^i}J\left(n_w+n_t\right)\right)_t-\Delta t\,\frac{\rho_w}{\rho_w^i}n_w\,\frac{\partial\delta P_w}{\partial\vec{x}}\overrightarrow{V_w}\right]dV&\\+\Delta t\int_S\delta P_w\left(\frac{\rho_w}{\rho_w^i}n_w\vec{n}\cdot\overrightarrow{V_w}\right)dS=0&\end{aligned} \qquad \text{(B.7)}$$

The discretized equilibrium equations together with the continuity formulation for a wetting fluid in a porous media described above both define the state of the porous medium (Abaqus 2014 guide).

The same governing conservation equation for a single-phase flow assuming a liquid with small compressibility $\left(c_f\right)$ applies.

$$\frac{\partial(\phi\rho)}{\partial t} = \nabla(\rho\upsilon) + q \qquad P \subset \Omega \tag{B.8}$$

$$\rho = \rho_i e^{\left[c_f\left(p-p_i\right)\right]} \tag{B.9}$$

However, the discretization approach for the finite element method is different from the finite difference method employed as shall be seen shortly. Assuming general natural boundary conditions

$$\begin{array}{lll} P = P_b & & P \subset \Gamma_2 \\ P = P_i & \text{for} & t = 0 \\ q = q_b & & q \subset \Gamma_1 \end{array} \tag{B.10}$$

Where Ω is the entire model domain, while Γ_1 and Γ_2 are the boundary regions where the flow rate and pressure boundary conditions are respectively defined. Discretization of the fluid flow equation by applying the concept of the Galerkin orthogonality using the residual method with a transposed arbitrary weight functions (w) yields

$$\int w^T \left(\nabla(\rho\upsilon) + \frac{\partial\left(V_{pore}\rho\right)}{\partial t} + q \right) d\Omega + \int_{\Gamma_1} w^T \left(-q + \bar{q}\right) d\Gamma + \int_{\Gamma_2} w^T \left(p - \bar{p}\right) d\Gamma = 0 \tag{B.11}$$

Assuming that the unknown variable is the pressure, then the pressure boundary integral on the boundary region is satisfied $\left(\int\limits_{\Gamma_2} w^T \left(p - \overline{p} \right) d\Gamma = 0 \right)$.

Let the arbitrary weight function be replaced by finite element shape functions as follows:

$$\begin{aligned} w &= N \\ \nabla w &= B \end{aligned} \tag{B.12}$$

Hence, the Galerkin orthogonality for the fluid flow formulation in term of pore volume $\left(V_{pore}\right)$ becomes:

$$\begin{gathered} \int w^T \left(\nabla \left(\rho \upsilon \right) \right) d\Omega + \int\limits_{\Gamma_1} w^T \left(-q + \overline{q} \right) d\Gamma + \int w^T \left(\frac{\partial \left(\phi \rho \right)}{\partial t} + q \right) d\Omega = 0 \\ \left[\int N^T \left(\nabla \left(\rho \upsilon \right) \right) d\Omega \right] + \int\limits_{\Gamma_1} N^T \left(-q + \overline{q} \right) d\Gamma + \left[\int N^T \left(\frac{\partial \left(\rho V_{pore} \right)}{\partial t} \right) d\Omega \right] + \int N^T q d\Omega = 0 \end{gathered} \tag{B.13}$$

The discretization of the pore volume rate of change term $\left(\int N^T \left(\frac{\partial \left(\rho V_{pore} \right)}{\partial t} \right) d\Omega \right)$ above can be obtained in a variety of ways. For this study, it is obtained according with the small liquid compressibility assumption and by the chain rule according to the following formulation

$$\left[\int N^T \frac{\partial}{\partial t} \left(\rho V_{pore} \right) d\Omega \right] = \int N^T \rho V_{pore} c_f \frac{\partial P}{\partial t} d\Omega + \int N^T \rho \left(\frac{\partial V_{pore}}{\partial t} \right) d\Omega \tag{B.14}$$

For isotropic problems, the pore volume $\left(V_{pore}\right)$ itself is defined as follows:

$$\begin{gathered} \delta V_{pore} = \left(1 - \frac{c_m}{c_b} \right) \delta \nabla u + \left(1 - \frac{c_m}{c_b} - \phi \right) c_m \delta P \\ \therefore \frac{\partial V_{pore}}{\partial t} = \left(1 - \frac{c_m}{c_b} \right) \frac{\partial}{\partial t} \left(\nabla u \right) + \left(1 - \frac{c_m}{c_b} - \phi \right) c_m \frac{\partial P}{\partial t} \end{gathered} \tag{B.15}$$

The pore volume discretization then becomes

$$
\begin{aligned}
&\left[\int N^T \frac{\partial}{\partial t}\left(\rho V_{pore}\right) d\Omega\right] \\
&= \int N^T \rho V_{pore} c_f \frac{\partial P}{\partial t} d\Omega + \int N^T \rho \left(\left(1-\frac{c_m}{c_b}\right)\frac{\partial}{\partial t}\left(\nabla u\right) + \left(1-\frac{c_m}{c_b}-\phi\right) c_m \frac{\partial P}{\partial t}\right) d\Omega \\
&= \int N^T \rho V_{pore} c_{f\Theta} N\dot{P}^e d\Omega + \int N^T \rho_\Theta \left(\left(1-\frac{c_m}{c_b}\right)\nabla N \delta \dot{u}^e + \left(1-\frac{c_m}{c_b}-\phi\right) c_m N\dot{P}^e\right) d\Omega \qquad \text{(B.16)} \\
&= \rho V_{pore} c_{f\Theta} \int N^T N d\Omega \dot{P}^e + \\
&\rho_\Theta \left(1-\frac{c_m}{c_b}\right) \int N^T \nabla N d\Omega \delta \dot{u}^e + \rho_\Theta \left(1-\frac{c_m}{c_b}-\phi\right) c_m \int N^T N d\Omega \dot{P}^e
\end{aligned}
$$

By the Gauss divergence theorem, in terms of the unit normal ($\vec{n}$), chain rule and substituting in the descritized pore volume term, the discretized fluid flow equation is transformed to become:

$$
\begin{aligned}
&\left[\int N^T \left(\nabla\left(\rho \upsilon\right)\right) d\Omega\right] + \int_{\Gamma_1} N^T \left(-q+\overline{q}\right) d\Gamma + \left[\int N^T \left(\frac{\partial\left(\rho V_{pore}\right)}{\partial t}\right) d\Omega\right] + \int N^T q d\Omega = 0 \\
&\therefore \left[\int N^T \left(\rho \upsilon^T \cdot \vec{n}\right) d\Gamma - \int \left(\nabla N\right)^T \left(\rho \upsilon\right) d\Omega\right] + \int_{\Gamma_1} N^T \left(-q+\overline{q}\right) d\Gamma + \int N^T q d\Omega + \left[\int N^T \left(\frac{\partial\left(\rho V_{pore}\right)}{\partial t}\right) d\Omega\right] = 0 \\
&\therefore \left[\int_{\Gamma_1} N^T q d\Gamma + \int \left(\nabla N\right)^T T \left(\nabla N\right) d\Omega P^e\right] + \int_{\Gamma_1} N^T \left(-q+\overline{q}\right) d\Gamma + \int N^T q d\Omega + \left[\int N^T \left(\frac{\partial\left(\rho V_{pore}\right)}{\partial t}\right) d\Omega\right] = 0 \qquad \text{(B.17)} \\
&\therefore \int_{\Gamma_1} N^T \overline{q} d\Gamma + \int \left(\nabla N\right)^T T \left(\nabla N\right) d\Omega P^e + \int N^T q d\Omega + \\
&\left[\rho V_{pore} c_{f\Theta} \int N^T N d\Omega \dot{P}^e + \rho_\Theta \left(1-\frac{c_m}{c_b}\right) \int N^T \nabla N d\Omega \delta \dot{u}^e + \rho_\Theta \left(1-\frac{c_m}{c_b}-\phi\right) c_m \int N^T N d\Omega \dot{P}^e\right] = 0
\end{aligned}
$$

Where $\rho V_{pore} c_{f_\Theta}$ is evaluated at the element center. The displacement, $\left(\frac{\partial u}{\partial t}\right)^e = \dot{u}^e$, and pressure, $\left(\frac{\partial P}{\partial t}\right)^e = \dot{P}^e$, partial derivatives are evaluated at the nodal point and can be moved outside of the intergrals while the transmissibility term evaluated upstream(up), $T = \frac{\rho k \delta K}{\mu}$, for stability and is introduced for convenience. The pressure is implicitly evaluated. Therefore, the final discretized form of the fluid flow equations in the finite element framework becomes:

$$\begin{gathered}\int_{\Gamma_1} N^T \overline{q} d\Gamma + \left\{ \frac{\rho k \delta}{\mu}_{up} \int \left(\nabla N\right)^T K \left(\nabla N\right) d\Omega_{up} \right\} P^e + \int N^T q d\Omega + \\ \left[\left\{ \rho V_{pore} c_{f\Theta} \int N^T N d\Omega \right\} \dot{P}^e + \left\{ \rho_\Theta \left(1 - \frac{c_m}{c_b}\right) \int N^T \nabla N d\Omega \right\} \delta \dot{u}^e + \left\{ \rho_\Theta \left(1 - \frac{c_m}{c_b} - \phi\right) c_m \int N^T N d\Omega \right\} \dot{P}^e \right] = 0\end{gathered} \tag{B.18}$$

Since the volume of integration of the source and sink terms are simply production and injection from fluid wells, the line integration approximation applies such that

$$\int N^T q d\Omega \approx \int N^T q dl \tag{B.19}$$

In customary matrix form, the final discretized form of the fluid flow equations within the Lagrange finite element framework becomes:

$$K^e \left(P^e\right)^{n+1} + S\left(u^e\right)^{n+1} = F_q{}^e + F_Q{}^e \tag{B.20}$$

where

$$\begin{gathered}\overline{K}^e = \frac{\rho k \delta}{\mu}_{up} \int \left(\nabla N\right)^T K \left(\nabla N\right) d\Omega_{up} + \\ \frac{\rho V_{pore} c_{f\Theta}}{\Delta t} \int N^T N d\Omega + \frac{\rho_\Theta \left(1 - \frac{c_m}{c_b} - \phi\right) c_m}{\Delta t} \int N^T N d\Omega \\ S = \rho_\Theta \left(1 - \frac{c_m}{c_b}\right) \int N^T \nabla N d\Omega \\ F_q{}^e = -\int N^T q dl \\ F_Q{}^e = -\int_{\Gamma_1} N^T \overline{q} d\Gamma\end{gathered} \tag{B.21}$$

Where $\overline{K}$ is the transmissibility-pore volume term, S is the compressibility-pore volume term, while F_q^e and F_Q^e sink-source well and boundary terms respectively.

B.2 Geomechanics

Assuming a homogenous, isotropic and symmetric material with a very small strain compared to unity, the geomechanical force equilibrium equation states that the gradient of the total stress tensor is balanced by the sum of all the body force which accounts for gravity.

$$\nabla.\vec{\sigma} - B = 0 \tag{B.22}$$

The discretized equilibrium statement for a porous medium is defined in Abaqus by the principle of virtual work for the volume under consideration in its current configuration at a given time.

$$\begin{gathered}
\int_V \vec{\sigma} : \delta\vec{\varepsilon} dV = \delta\vec{\mathrm{v}} \left[\int_S \vec{t}\, dS + \int_V \vec{f} dV + \int_V \left[n_f \gamma_w \right] dV \right] \\
\delta\vec{\mathrm{v}} = \vec{\mathrm{N}}^N \delta\mathrm{v}^N \\
\delta\vec{\varepsilon} = \beta^N \delta\mathrm{v}^N = sym\left(\frac{\partial\delta\vec{\mathrm{N}}^N}{\partial\vec{\mathrm{x}}} \right)
\end{gathered} \tag{B.23}$$

Where γ_w is the specific gravity of the wetting fluid, $\vec{\sigma}$ is the Cauchy stress, $\vec{t}$ are the surface tractions per unit area (S), n_f is the total volume of wetting fluid (free plus trapped) per unit volume in the current configuration, $\vec{f}$ is the body force per unit volume (V) while $\delta\vec{\mathrm{V}}$ and $\delta\vec{\varepsilon}$ are respectively the virtual velocity field and the virtual rate of deformation both of which are a function of the Lagrangian framework interpolation function $\left(\vec{\mathrm{N}}^N\right)$. The most general statement of the virtual work principle with assumed independent incremental virtual velocity field, $\delta\mathrm{v}$, can then be expressed more familiarly as a balance between internal (I^N) and external (P^N) acting force arrays such that the virtual velocity field cancels out as seen below:

$$\begin{gathered}\delta \mathrm{v}\int_V \vec{\sigma} : \delta\vec{\varepsilon}\, dV = \delta \mathrm{v}\left[\int_S \vec{t}\ dS + \int_V \vec{f} dV + \int_V \left[n_f \gamma_w \right] dV \right] \\ \delta \mathrm{v}^N I^N = \delta \mathrm{v}^N P^N \\ I^N + \left(-P^N \right) = 0 \end{gathered} \tag{B.24}$$

For this study, the virtual work principle can be applied such that for a body in equilibrium with gravitational body forces and applied forces, the sum of energy of the applied loads due to external work (δW) and the strain energy stored (δU) during the virtual displacement of the domain should sum up to zero.

$$\delta W + \delta U = 0 \tag{B.25}$$

Using the same shape functions as done in the fluid flow module,$(N\ and\ B)$, of the Lagrangian finite element framework, the displacement (u), strain (ε) and net stress (σ_{net}) are discretized as follows:

$$\begin{gathered} \delta u = N \delta u^e \\ \delta\varepsilon = \nabla \delta u = \nabla N \delta u^e = B \delta u^e \\ \delta\sigma_{net} = \vec{C}\delta\varepsilon - \left(I - \frac{1}{3} c_m \right) \bar{I} p = \vec{C} B \delta u^e - \left(I - \frac{1}{3} c_m \right) \bar{I} N \bar{p}^e \end{gathered} \tag{B.26}$$

Where

$$I = \begin{bmatrix} 1 & 0 & 0 & 0 & 0 & 0 \\ 0 & 1 & 0 & 0 & 0 & 0 \\ 0 & 0 & 1 & 0 & 0 & 0 \\ 0 & 0 & 0 & 1 & 0 & 0 \\ 0 & 0 & 0 & 0 & 1 & 0 \\ 0 & 0 & 0 & 0 & 0 & 1 \end{bmatrix} \tag{B.27}$$

$$c_m = \frac{3\left(1-2\nu_m\right)}{E_m}$$

$$\overline{I} = \begin{bmatrix} 1 & 1 & 1 & 0 & 0 & 0 \end{bmatrix}^T$$

Considering a virtual displacement at the (δu^e) nodes, the work done (δW) due to external surface stress (T) and the strain energy (δU) stored in the entire domain become

$$\begin{aligned} \delta W &= \int_{S^e} \left(\delta u\right)^T T d\Gamma \\ \delta U &= \int_{V^e} \left(\delta \varepsilon^T \sigma_{net} - \delta u^T F\right) d\Omega \end{aligned} \tag{B.28}$$

Hence for equilibrium in terms of the introduced shape functions

$$\begin{gathered} \left[\int_{S^e} \left(\delta u\right)^T T d\Gamma\right] + \left[\left\{\int_{V^e} \delta\varepsilon^T \left(\sigma_{net}\right) d\Omega\right\} - \left\{\int_{V^e} \delta u^T F d\Omega\right\}\right] = 0 \\ \left[\left(\delta u^e\right)^T \int_{S^e} N^T T d\Gamma\right] + \left[\left(\delta u^e\right)^T \left\{\int_{V^e} B^T \left(\vec{C} B \delta u^e - \left(I - \frac{1}{3} c_m\right) \overline{I} N \overline{p}^e\right) d\Omega\right\} - \left\{\left(\delta u^e\right)^T \int_{V^e} N^T F d\Omega\right\}\right] = 0 \\ \left[\int_{S^e} N^T T d\Gamma\right] + \left[\left\{\int_{V^e} B^T \vec{C} B \delta d\Omega\right\} u^e - \left\{\int_{V^e} B^T \left(I - \frac{1}{3} c_m\right) \overline{I} N d\Omega\right\} \overline{p}^e - \int_{V^e} N^T F d\Omega\right] = 0 \end{gathered} \tag{B.29}$$

Therefore, the final discretized form of the geomechanics equations in the finite element framework becomes:

$$\left\{ \int_{V^e} B^T \vec{C} B \delta d\Omega \right\} u^e - \left\{ \int_{V^e} B^T \left(I - \frac{1}{3} c_m \right) \overline{I} N d\Omega \right\} \overline{p}^e = \int_{V^e} N^T F d\Omega - \int_{S^e} N^T T d\Gamma \qquad \text{(B.30)}$$

In customary matrix form, the final discretized form of the geomechanics equations within the Lagrange finite element framework for a master element (^{e})becomes:

$$K^e \left(u^e \right) - H^e \left(\overline{p}^e \right) = F^e + T^e \qquad \text{(B.31)}$$

$$\text{where} \quad \begin{aligned} K^e &= \int_{V^e} B^T \vec{C} B \delta d\Omega \\ H^e &= \int_{V^e} B^T \left(I - \frac{1}{3} c_m \right) \overline{I} N d\Omega \\ F^e &= \int_{V^e} N^T F d\Omega \\ T^e &= \int_{S^e} N^T T d\Gamma \end{aligned} \qquad \text{(B.32)}$$

Where K^e is the bulk stiffness term, H^e matrix (effective) stiffness term, while F^e and T^e body force and nodal traction force load terms respectively. When the above fundamental geomechanics elasticity equations are assembled for all the finite elements in the domain, a set of linear equations can be solved with respect to the nodal displacements.

B.3 Fully Coupled Coupling Using Finite Element Approach

The fully coupled finite element coupled strategy in Abaqus is detailed in various literature. An extensive Lagrange finite element formulation can be found in the course material for “finite element method for geomechanics problems in oil industries” at Texas A&M University (Morita 2015). Abaqus employs the finite element method using gauss integration point formulation, interpolated shape functions, and backward Euler approximation to simultaneously solve a system of equations both pressure and displacement. However, only parts pertinent to the coupled fluid flow-geomechanics formulation conducted in this study are provided within the context and scope of the current study. It is important to note the temperature effects have been neglected within the scope of the current study and only pressure terms are included in the above discretization. The discretized final system of equations for the fluid flow and geomechanics are fully coupled and numerical solved simultaneously by imposing time stepping on a grid to obtain the discrete pressure and displacement unknowns as shown below

$$\begin{aligned} &\bar{K}^{e}\left(P^{e}\right)^{n+1}+S\left(u^{e}\right)^{n+1}=F_{q}^{\ e}+F_{Q}^{\ e}---FluidFlow \\ &K^{e}\left(u^{e}\right)-H^{e}\left(\bar{p}^{e}\right)=F^{e}+T^{e}---Geomechanics \end{aligned} \tag{B.33}$$

Where the matrix coefficients from the fluid flow and geomechanics formulation are derived in Appendix B.1 and B.2. The fully coupled approach used in Abaqus is different from the two-way iteratively coupled approach because the pressure and displacement unknown variables are solved simultaneously using discretized matrix equations instead of a two-way feedback approach. A fully coupled solution is achieved through $\bar{K}^{e}$ and K along the coupling term diagonal.

APPENDIX C

UNIT CONVERSION- CMG VS ABAQUS

C.1 Unit Tables

Care must be taken when working with input values and units across different softwares. In general CMG uses field units. However, there are a few exceptions where SI units are used as is the case for temperature and flowrate as stated in the simulation manuals. For coupled diffusion-displacement problems in Abaqus Standard, care was taken when choosing the units of the problem for consistency. This is because the coupled equations may be numerically ill-conditioned if the choice of units are mixed thereby causing the output values generated by equations from two different fields to differ by many orders of magnitude. In general, the International System of units (SI) were used for all Abaqus inputs in this study. Fig C.1 below summarizes a few of the key unit conversion factors and tables which are relevant for the study in this thesis.

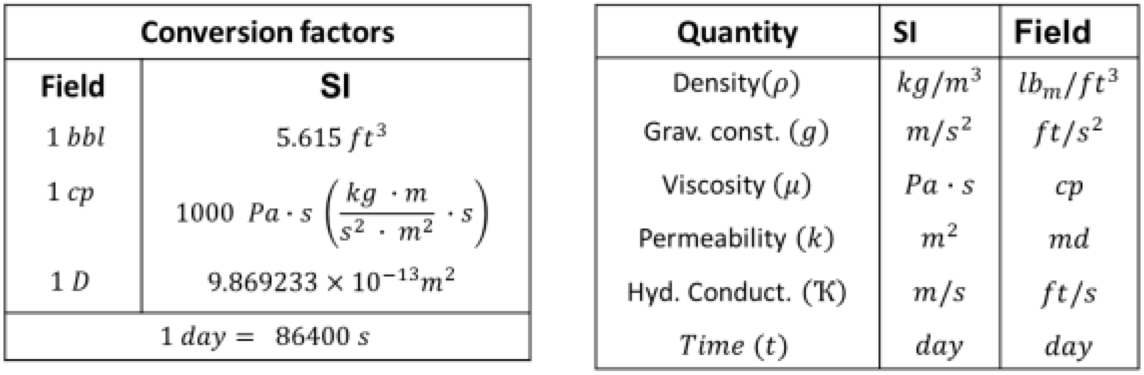

Conversion factors	
Field	**SI**
$1\ bbl$	$5.615\ ft^3$
$1\ cp$	$1000\ \ Pa \cdot s\ \left(\frac{kg\ \cdot m}{s^2\ \cdot\ m^2}\ \cdot s\right)$
$1\ D$	$9.869233 \times 10^{-13} m^2$
$1\ day = \ \ 86400\ s$	

Quantity	SI	Field
Density(ρ)	kg/m^3	lb_m/ft^3
Grav. const. (g)	m/s^2	ft/s^2
Viscosity (μ)	$Pa \cdot s$	cp
Permeability (k)	m^2	md
Hyd. Conduct. ($\mathcal{K}$)	m/s	ft/s
$Time\ (t)$	day	day

Fig. C.1 – Conversion Factor and Unit Tables Summary

C.2 Hydraulic Conductivity-Permeability Sample Conversion

A good example of when care of unit consistency must be exercised is the conversion between permeability in CMG to the hydraulic conductivity in Abaqus. As seen in chapter 2, Forchheimer’s law is a more general form of a more specific Darcy’s law (low velocity flow only) which describes porous media fluid flow. Fig C.2 compares the similarities between both porous media fluid flow laws and the connection between hydraulic conductivity and permeability. Forchheimer equations are on the left while Darcy’s law equations are on the right side of the figure below.

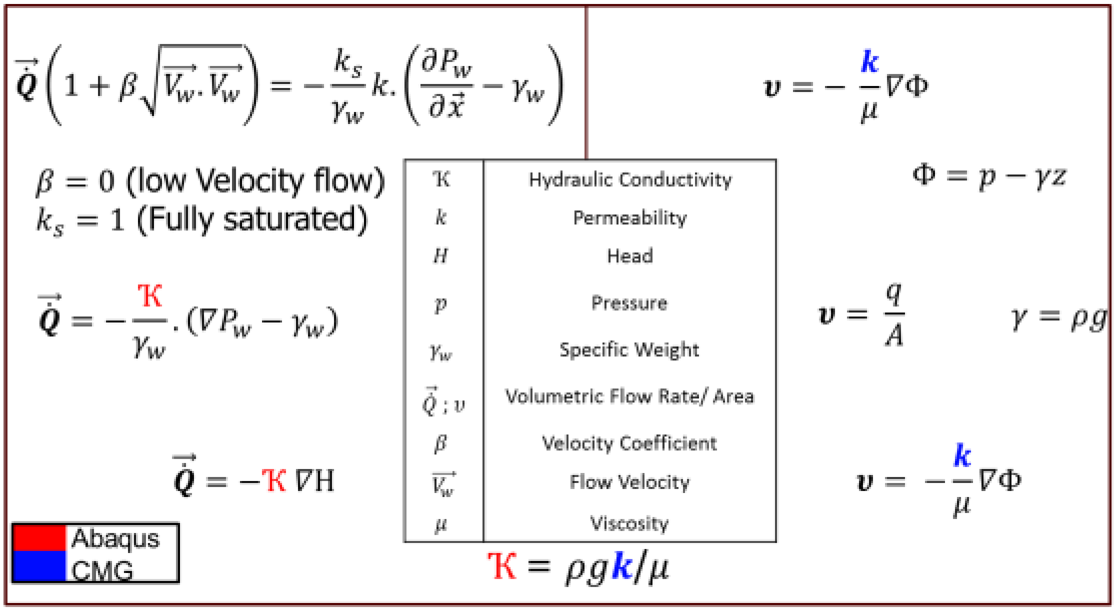

$$\vec{Q}\left(1+\beta\sqrt{\vec{V_w}.\vec{V_w}}\right) = -\frac{k_s}{\gamma_w}k.\left(\frac{\partial P_w}{\partial \vec{x}} - \gamma_w\right)$$

$$v = -\frac{k}{\mu}\nabla\Phi$$

$\beta = 0$ (low Velocity flow)
$k_s = 1$ (Fully saturated)

$Ϗ$	Hydraulic Conductivity
k	Permeability
H	Head
p	Pressure
γ_w	Specific Weight
$\vec{Q}\,;\,v$	Volumetric Flow Rate/ Area
β	Velocity Coefficient
$\vec{V_w}$	Flow Velocity
μ	Viscosity

$$\Phi = p - \gamma z$$

$$\vec{Q} = -\frac{Ϗ}{\gamma_w}.(\nabla P_w - \gamma_w)$$

$$v = \frac{q}{A} \qquad \gamma = \rho g$$

$$\vec{Q} = -Ϗ\,\nabla H$$

$$v = -\frac{k}{\mu}\nabla\Phi$$

🟥 Abaqus
🟦 CMG

$$Ϗ = \rho g k/\mu$$

Fig. C.2 – Forchheimer-Darcy Law Comparison

Fig C.3 below illustrates the correct unit conversion in detail which comes from comparison between the Forchheimer and Darcy laws for porous media fluid flow. The conversion factors for the respective units are summarized in Fig C.1

$$K\left(\frac{m}{day}\right) = \frac{\rho\left(\frac{kg}{m^3}\right) \times g\left(\frac{m}{s^2}\right) \times k(md) \left| \frac{1\ D}{1000\ md} \times \frac{9.869233\times10^{-13}\ m^2}{1\ D} \right|}{\mu(cp) \left| \frac{1\ Pa\cdot s}{1000\ cp} \times \frac{1\ \frac{kg\cdot m}{s^2\cdot m^2}\cdot s}{1\ Pa\cdot s} \right|} \times \left| \frac{24\ hr \times \left| \frac{60\ min}{1\ hr} \right| \times \left| \frac{60\ sec}{1\ min} \right|}{1\ day} \right|$$

Fig. C.3 – Hydraulic Conductivity- Permeability Conversion